Clim Dyn (2013) 41:1899–1922
DOI 10.1007/s00382-012-1598-3

A regional modeling study of the diurnal cycle in the lower troposphere in the south-eastern tropical Pacific

Thomas Toniazzo · Fengpeng Sun · Carlos R. Mechoso · Alex Hall

Received: 28 June 2012 / Accepted: 12 November 2012 / Published online: 28 November 2012

Abstract We examine the influence of the South-American land-mass and its mountains on the significant cyclic diurnal and semidiurnal components of the average circulation in the adjacent area of the southeastern tropical Pacific (SEP). Our approach is based on a number of numerical simulations with the regional atmospheric model weather research and forecasting forced by the National Centers for Environmental Prediction's final analysis operational analysis data. In the control simulation the model domain covers the SEP and a large part of South America. In several sensitivity experiments the domain is reduced to progressively exclude continental areas. We find that the mean diurnal cycle is sensitive to model domain in ways that reveal the existence of different contributions originating from the Chilean and Peruvian land-masses. The experiments suggest that diurnal variations in circulations and thermal structures over the SEP (mainly forced by local insolation) are influenced by convection over the Peruvian sector of the Andes cordillera, while the mostly dry mountain-breeze circulations force an additional component that results in semi-diurnal variations near the coast. A series of numerical tests, however, reveal sensitivity of the simulations to the choice of vertical grid, limiting the possibility of solid quantitative statements on the amplitudes and phases of the diurnal and semidiurnal components across the domain.

T. Toniazzo (✉)
Department of Meteorology, University of Reading,
PO Box 243, Reading, Berkshire RG6 6BB, UK
e-mail: t.toniazzo@reading.ac.uk

F. Sun · C. R. Mechoso · A. Hall
University of California, Los Angeles,
Los Angeles, CA, USA

Keywords Diurnal circulations · Diurnal cycle · Gravity waves · South-eastern Pacific

1 Introduction

The present study focuses on the southeastern tropical Pacific (SEP). This region, in the eastern side of the southern Pacific anticyclone under the sinking branch of the Hadley cell, is characterized by one of the most extended and persistent stratocumulus (Sc) cloud decks in the world. The clouds shield the ocean surface from solar radiation, and thus strongly influence the regional and global radiation budget. To the east and the north-east, the South-American land-mass rises steeply, forming the Andes Cordillera with heights reaching 5 km. The near-shore areas along the coasts of southern Peru and northern Chile have strong low-level southerly and southeasterly winds. These are linked to strong coastal upwelling and cold sea surface temperatures (SSTs). During the southern warm season, convection associated with the South American monsoon system and low-level heating over the Chaco Low region contribute to maintain large-scale subsidence and strong coastal winds (Rodwell and Hoskins 2001; Ma et al. 2010).

It has been shown that this circulation has important variations on diurnal time scales. According to Rutllant (1993) and Garreaud and Muñoz (2005), the southerly low-level jet off the west coast of subtropical South America has a strong diurnal cycle. Munoz (2008) used high-resolution satellite scatterometer and reanalysis data to investigate the variability of surface winds, pressure, temperature, and vertical velocity both in the boundary layer and the lower free troposphere off the Chilean coast. The results highlighted the importance of differential thermal forcing below

2,000 m in generating the diurnal cycle of the zonal geostrophic wind, as well as the diurnal acceleration and deceleration of the meridional wind in the boundary layer. The prevalence of a semidiurnal component along the Chilean coast was also noted.

Associated with the diurnal variations of the circulation is the well-known and radiatively important diurnal cycle of the marine stratocumulus cover. Globally, Minnis and Harrison (1984) and Rozendaal et al. (1995) found a pronounced diurnal variation of marine low cloudiness, with cloud amount reaching its maximum in the early or late morning in almost all locations of the world oceans. Similarly, Wood et al. (2002) reported a clear diurnal cycle in liquid-water path (LWP) retrieved from a two-year long record of satellite microwave radiometer data, with a peak in the early morning. O'Dell et al. (2008) provided confirmation of these results from an 18-year-long records of eight satellite-based passive microwave data. Accordingly, the diurnal cycle of LWP is often characterized by a double peak, suggesting the presence of a significant semidiurnal contribution with a especially strong amplitude very close to the Peruvian coastline in October. This double-peaked structure indicates that mechanisms other than the diurnal cycle of insolation are at work in determining the variability of circulation and clouds in the SEP at diurnal time scales.

Rozendaal et al. (1995) and Dai and Desser (1999) speculated that a large-scale diurnal cycle in divergence associated with the intense convection over the Andes Cordillera would result in a downwelling-upwelling wave forming off the Peru–Chile coasts and propagating westward to the open ocean. Wood et al. (2009) examined the differences in the diurnal cycles of surface divergence from reanalysis and scatterometer satellite data between oceanic locations both near and far away from the coast. They found propagation away from the coast with a phase speed $\sim$25 m/s, and a synochronous behavior with the diurnal solar irradiation over open-ocean areas, consistent with the expected area of influence of land-sea breeze systems (Rotunno 1983). The consequent downwelling waves cause a cloud response that propagates westward from the Andes Cordillera to a broad region of the SEP. Mapes et al. (2003) explicitly discussed the gravity-wave dynamics involved in land-sea breeze systems and their effect on adjacent oceanic areas in the Gulf of Panama. They demonstrated a connection between the diurnal cycle of deep convection over land, the sea/mountain breeze systems, and the gravity-wave pulses investing the oceanic region. They also found a dominant first diurnal harmonic with a propagation speed of 23 m/s, and timed as expected to coincide with the maximum in thermal forcing over the mountain ridge.

Though some locations in the SEP are relatively well sampled in ship-based field campaigns and remotely by satellites, few modeling studies have concentrated on the pronounced diurnal variations in the boundary layer circulation and cloudiness and their modulation by solar radiation and changes of surface divergence at the regional scale. Approaches based on numerical models are particularly challenging owing to difficulties in the simulation of the complex SEP geography and climate. Nevertheless, Garreaud and Munoz (2004) found broad agreement between the mean diurnal cycle of winds simulated by regional models and found in observations for three different seasons. Rahn and Garreaud (2010a) suggested that interference between remotely forced perturbations in the boundary layer (mainly from the Peruvian highlands) and the locally induced (radiatively driven) cycle leads to the appearance of the semidiurnal component over the SEP. However, the double-peaked structure of the diurnal variability in the circulation and clouds over the SEP has not been thoroughly investigated so far.

The present paper aims to a better understanding of the special combination of diurnal and semidiurnal features in the circulation and clouds over the SEP. We discuss the contributions to such features by several processes in different regions. The research approach is based on a suite of sensitivity experiments with a regional atmospheric model.

The remainder of the paper is organized as follows. Section 2 describes the regional atmospheric model, control and sensitivity experiments performed, and observational data sets used for model validation. Section 3 reviews the simulated mean climatology of the region (circulation, vertical stratification) and compares it with satellite and ship observations. Section 4 explores selected features of the diurnal cycles of the low-level circulation. Section 5 analyzes the results obtained in the sensitivity experiments, with a particular focus on the diurnal and semidiurnal variations of the circulation. Section 6 examines additional simulations using regional model configurations different from the standard one in order to evaluate the degree of robustness of previous results. Section 7 presents a general discussion and summary of the main results.

2 Model description and observational datasets

2.1 Numerical model

We use the advanced research version of the Weather Research and Forecasting (WRF) model (ARW, version 3.0.1). WRF is developed by National Center for Atmospheric Research (NCAR), and is a community mesoscale model designed for use on regional grids for a range of applications (Skamarock et al. 2008). It consists of a fully compressible nonhydrostatic dynamical core with high-order, conserving numerical techniques.

WRF offers a range of options for the parametrisation of sub-grid-scale processes.

Our set of choices is the following: Kain and Fritsch (1990) cumulus scheme; Purdue Lin microphysics scheme; Rapid Radiative Transfer Model (RRTM) longwave radiation (Mlawer et al. 1997); Dudhia shortwave radiation schemes (Dudhia 1989); Yonsei University (YSU) planetary boundary layer (PBL) scheme (Hong et al. 2006); and the NOAH Land Surface Model (Chen and Dudhia 2001) for land surface processes including vegetation, soil, snowpack and land atmosphere energy, momentum and moisture exchange.

The lateral boundary and initial conditions for the simulations are derived from the National Centers for Environmental Prediction's (NCEP) final analysis (FNL) fields at 1° × 1° resolution and 6 hourly interval. The boundary conditions are prescribed over a domain with the depth of 5 grid-cells where prognostic variables are relaxed towards the FNL solution. The sea surface temperatures (SST) are prescribed at the lower boundary from the daily-varying optimum interpolation SST (OISST) analysis (Reynolds and Smith 1994). The model grid has a central horizontal spacing of 45 km and 43 sigma levels in the vertical. In an attempt to better represent the sharp inversion at the top of the marine PBL, the vertical resolution is enhanced with 27 layers below about 800 hPa. The remaining 16 layers above this level are spaced nearly uniformly, with a vertical resolution between 50 and 60 hPa in the mid-troposphere. This is a common choice in previous studies of the SEP with this model (e.g. Rahn and Garreaud 2010a, b). Different configurations and their impact on the results are discussed in Sect. 6. All model diagnostics in our runs were stored at hourly intervals.

The model domain for the control simulation is shown in Fig. 1. This domain includes much of the South American land mass. The domains are smaller in the three additional simulations discussed in Sect. 5, with changes in the position of the eastern boundary such as to exclude part or all of the Andes. Each simulation is initialized from 00UTC, October 14, 2006 and the last fifteen days of October are evaluated in this study.

2.2 Observations

For validation purposes, model results are compared to a series of observational and reanalysis datasets. The 2006 NOAA Stratus research cruise with the RV Ronald H. Brown (RHB), which took place between October 13–25 in the stratocumulus region off-shore of Chile and Peru, provided continuous ship-based measurements of surface meteorology, turbulent and radiative fluxes, cloud thickness and optical properties. Rawinsondes were launched from the ship every 4 or 6 h beginning October 18, providing vertical profiles of air temperature, humidity, and winds. We also use QuickSCAT (Centre ERS d'Archivage et de Traitement 2002; Jet Propulsion Laboratory 2000) scatterometer daily-mean surface wind data on a 0.5° × 0.5° grid. Finally, we use reanalysis data from the ERA-Interim project (Dee et al. 2011).

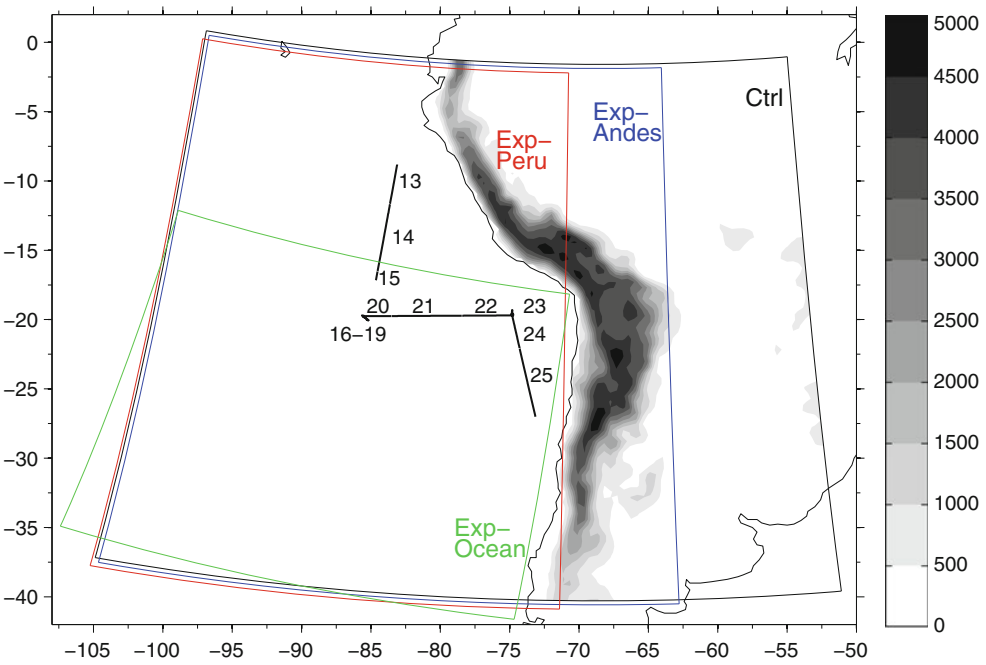

Fig. 1 Map of topographic elevations (*shaded*, in metres) for the study area. Superimposed are the transects of ship-based balloon soundings with the corresponding observing locations and dates of October 2006, and the simulation domain for the WRF control integration (*black box* labelled "Ctrl") and for the sensitivity experiments (*coloured lines* and labels)

Figure 1 also shows the locations and dates along the ship tracks where soundings were made in October 2006. The westernmost and easternmost points along 20S correspond to the locations of two oceanographic buoys: the Woods Hole Oceanographic Institution (WHOI) Stratus Ocean Reference Station buoy at 85 W, 20S, and the Deep-Ocean Assessment and Reporting of Tsunami (DART) at 75 W, 20S, respectively.

3 Simulated mean circulation

We briefly summarize the mean atmospheric circulation in the SEP (Wyant et al. 2010; Rahn and Garreaud 2010a, b; Toniazzo et al. 2011; Yang et al. 2011). Southerly to south-easterly winds prevail between the surface and 700 hPa, veering towards westerlies above that level. The meridional component also changes sign, reflecting the regional imprint of the Hadley circulation. Moving away from the coast (westwards and south-westwards), the isoentropes rise with a concomitant increase in cloud-top and boundary-layer heights. In the upper portion of the MBL near the coast, a prominent feature is the southerly low-level jet, with a maximum wind core near 950 hPa at 30S.

The WRF simulations broadly capture all of these features. Figure 2 compares the mean zonal and meridional 10-m winds with QuikSCAT data averaged over the simulated period. In general there is good agreement both in strength and spatial pattern. The visible difference between simulated and observed zonal wind near the WHOI buoy in the center of the domain (85 W, 20S) amounts to an overestimation of about 10 %. Along the Peruvian and Chilean coastline the simulated zonal wind has a westerly bias. The southerly low-level jet along the Chilean coastline is overestimated by the model. The bias in this case is as large as 2 ms^{-1}, a significant fraction of the observed mean value of about 8 ms^{-1}. The errors in the simulated zonal and meridional surface wind component are therefore larger along the coastline than over the open ocean.

The vertical cross-sections of potential temperature and winds in Fig. 3 show differences between the WRF simulation and the ERA-Interim reanalysis. The sections are along 21S and 73.5 W, and are roughly perpendicular and parallel to the Chilean coastline, respectively. The warm error in the lower troposphere (Fig. 3a, b) indicates that near the coast the simulated inversion is too close to the surface. Although the reanalysis itself is uncertain, such underestimation of the inversion height is a well-known problem in simulations for this area (Wyant et al. 2010; Rahn and Garreaud 2010a; Yang et al. 2011). The model difficulties lessen seawards of 85 W or poleward of 26S. A westerly wind-shear error between 900 and 700 hPa is visible in panel (d). The simulated ascent and descent are

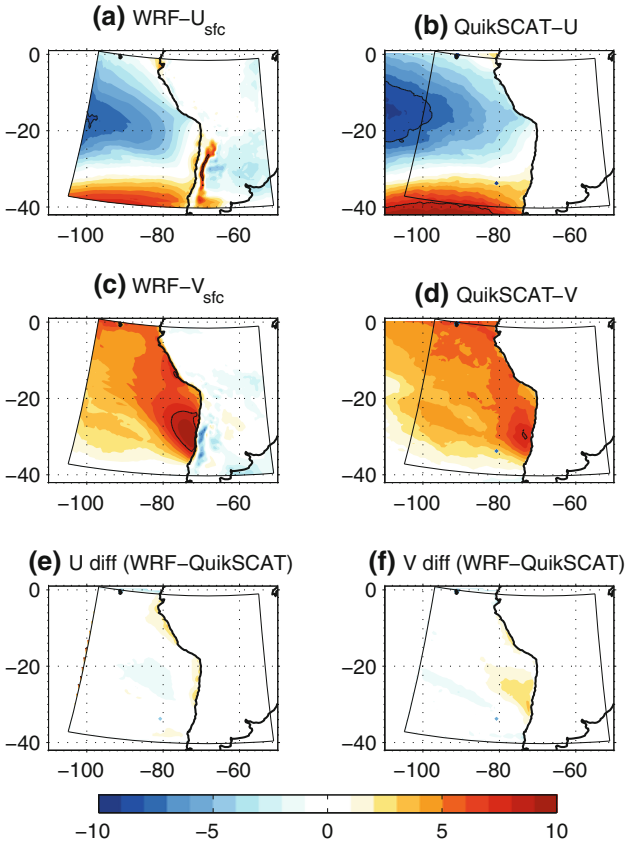

Fig. 2 Mean **a** zonal wind for WRF and **b** QuikSCAT, **c** meridonal wind for WRF and **d** QuikSCAT, **e** zonal wind difference and **f** meridional wind difference. Contour of ±8 m/s are highlighted

both stronger than in the reanalysis, although the agreement is fairly good over the ocean area and below the level of the orographic ridge.

In Fig. 4 we compare individual temperature and moisture profiles from the simulation with ship-based observations at the locations of the WHOI (20S, 85 W) and DART (20S, 75 W) buoys made in October 16–19 and October 23, respectively (cf. Fig. 1). Figure 4a and b show an inversion strength of 10–15 K above the well-mixed MBL at both sites. It is located at a height of roughly 1,100 m at 75 W, rising to 1,800 m at 85 W, consistent with the mean zonal gradient in PBL depth. The simulation reproduces the observed temperature inversion and its zonal tilt, but the boundary layer height is underestimated by about 200–300 m. Within the boundary layer, the simulation has a cool bias of about 1–2 K. Figure 4c and d show the vertical profiles of specific humidity at both buoy sites, highlighting the reduced cloud-top height compared with observations. Apart from the low height bias, the simulation generally matches the observed moisture structure in the vertical column at the WHOI buoy. At the DART buoy site, however, the simulation also overestimates the moisture content in the mid-troposphere. This is

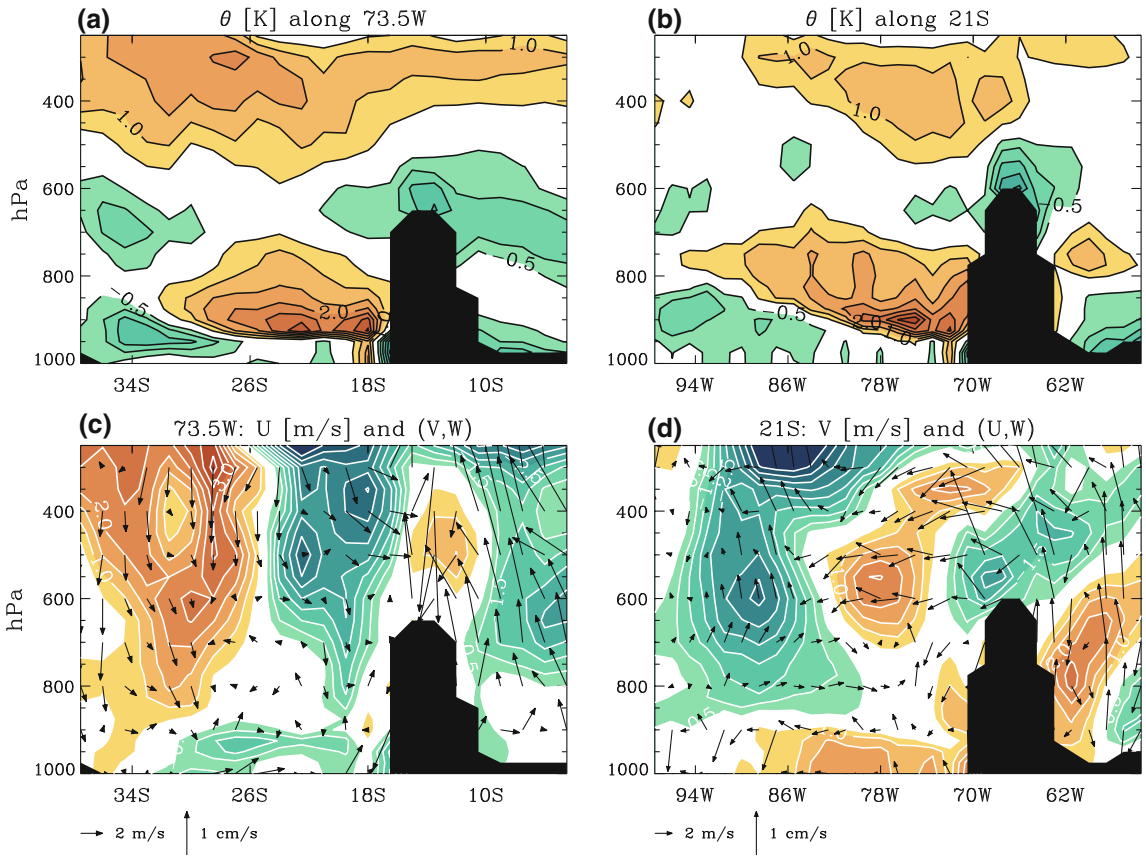

Fig. 3 Height-latitude (**a**, **c**) and height-longitude (**b**, **d**) cross-sections showing differences between the control simulation and ERA-Interim reanalysis. **a**, **b** Potential temperature (contour spacing 0.5 K, zero line omitted). **c**, **d** Wind components (m/s for the horizontal components, cm/s for the vertical wind). WRF data is subsampled to the spatial and temporal resolution of the reanalysis product

also a common bias of atmospheric circulation models in this area (Wyant et al. 2010; Medeiros et al. 2012).

4 Diurnal variability

4.1 General

Figure 5 shows the simulated anomalies, defined as the composite deviations from the daily mean, of the zonal wind on a longitude-height section along 20S and at different times of the mean diurnal cycle. Note that local time (LT) is UTC-4 in Chile, UTC-5 in Peru and at the DART buoy, and UTC-6 at the WHOI buoy.

Anomalous onshore westerlies appear first at 18:00 UTC just off the coast in the lower troposphere, and peak later at 00:00 UTC with a maximum at 850 hPa. These westerly anomalies gradually vanish, and anomalous offshore easterlies become dominant over the ocean from 9:00 UTC to 15:00 UTC. The maximum diurnal amplitude of the anomalous zonal wind occurs around 700–900 hPa, just above the MBL top. On the eastern side of the Andes, zonal wind anomalies are nearly out of phase with those over the ocean to the west. This feature is consistent with a strong diurnal cycle of divergence anomalies over the Andes. There is anomalous convergence in the late afternoon, associated with anomalous ascending motion over the Andes, and divergence in the early morning associated with anomalous descending motion.

The simulated meridional wind anomalies are shown in Fig. 6 on a latitude-height section along 73 W. The coastal jet between the surface and 800 hPa, seen in Fig. 2, displays a prominent diurnal cycle too. The southerly jet strengthens first around mid-afternoon 21:00 UTC (16:00 LT), and reaches its peak magnitude in the early evening 00:00 UTC (19:00 LT). The jet weakens around late morning 15:00 UTC (10:00 LT). The maximum amplitude of the diurnal wind anomaly occurs at around 25S.

We next examine the diurnal variability near the top of the MBL and at the surface. Figure 7 shows maps of the simulated mean diurnal variations of vertical velocity above the boundary layer at 800 hPa every 2 h. In general,

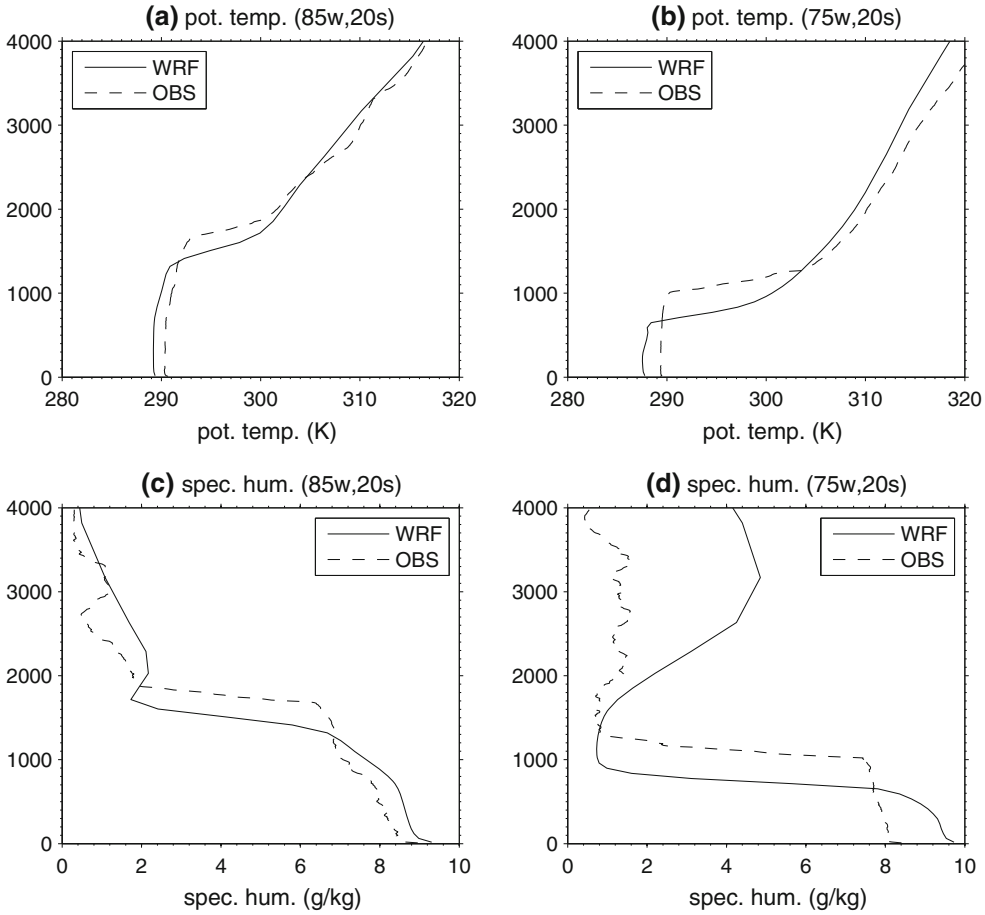

Fig. 4 Mean vertical profiles of **a** potential temperature (K), **c** specific humidity (g/kg) and **e** cloud liquid water (g/kg) at the WHOI buoy (85 W, 20S). **b**, **d** and **f** are for the location of the DART buoy (75 W, 20S)

there is subsidence over most oceanic areas, with increasingly stronger magnitudes offshore and towards the south of the domain. Added to the mean subsidence Fig. 7 shows a zone of positive vertical wind that is aligned with the coast and propagates from land towards the open ocean over a substantial distance. Along the Peruvian coast, this band of ascending motion appears first around 18:00 UTC (13:00 LT) and persists over the next 3–4 h. This ascending motion is associated with the daytime heating of the western slopes of the Andes Cordillera (Rahn and Garreaud 2010a; Toniazzo et al. 2011). Along the Peruvian coast, the magnitude of this vertical motion reaches a maximum at around 22:00 UTC (17:00 LT). The area of ascending motion forms a band parallel to the Peruvian coast, and moves southwestward over the open ocean until around 12:00 UTC, when the anomaly becomes too weak to produce net ascent. Along the Peruvian and northern Chilean coast, descending motion develops after the ascending wave propagates offshore at 2:00 UTC (21:00–22:00 LT). This negative phase of the diurnal wave lasts for a longer time than the ascending one. In addition to the alternation between anomalous ascent and descent motions, Fig. 7 displays other interesting features of the diurnal cycle. At 8:00–10:00 UTC, for example, two clear bands of ascent indicate sub-diurnal variations. We will further discuss this feature in Sect. 5.

To further distinguish the contributions to the variability by diurnal and sub-diurnal components we perform at each location a harmonic analysis of the vertically integrated horizontal mass flux and its divergence at lower levels, i.e. between the surface and 800 hPa. This is shown in Fig. 8. Taken together, the diurnal (24 h) and semidiurnal (12 h) harmonics of the horizontal mass flux divergence explain more than 70 % of the total variance at sub-daily time-scales. The diurnal harmonic generally dominates the diurnal variability of near-surface divergence over open ocean (Fig. 8a).

Near the north-western edge of the domain, Equatorward of 15S and West of 85 W, diurnal anomalies are also associated with the global diurnal tide (Deser and Smith 1998; Takahashi 2012). This component is characterised by a large surface-pressure signature near the Equator and near-uniform zonal phase within our computational domain, and is easily distinguished from the gravity-waves originating from the coasts. Its contribution to the lower-tropospheric anomalies discussed in this paper is generally small and will be neglected in the following.

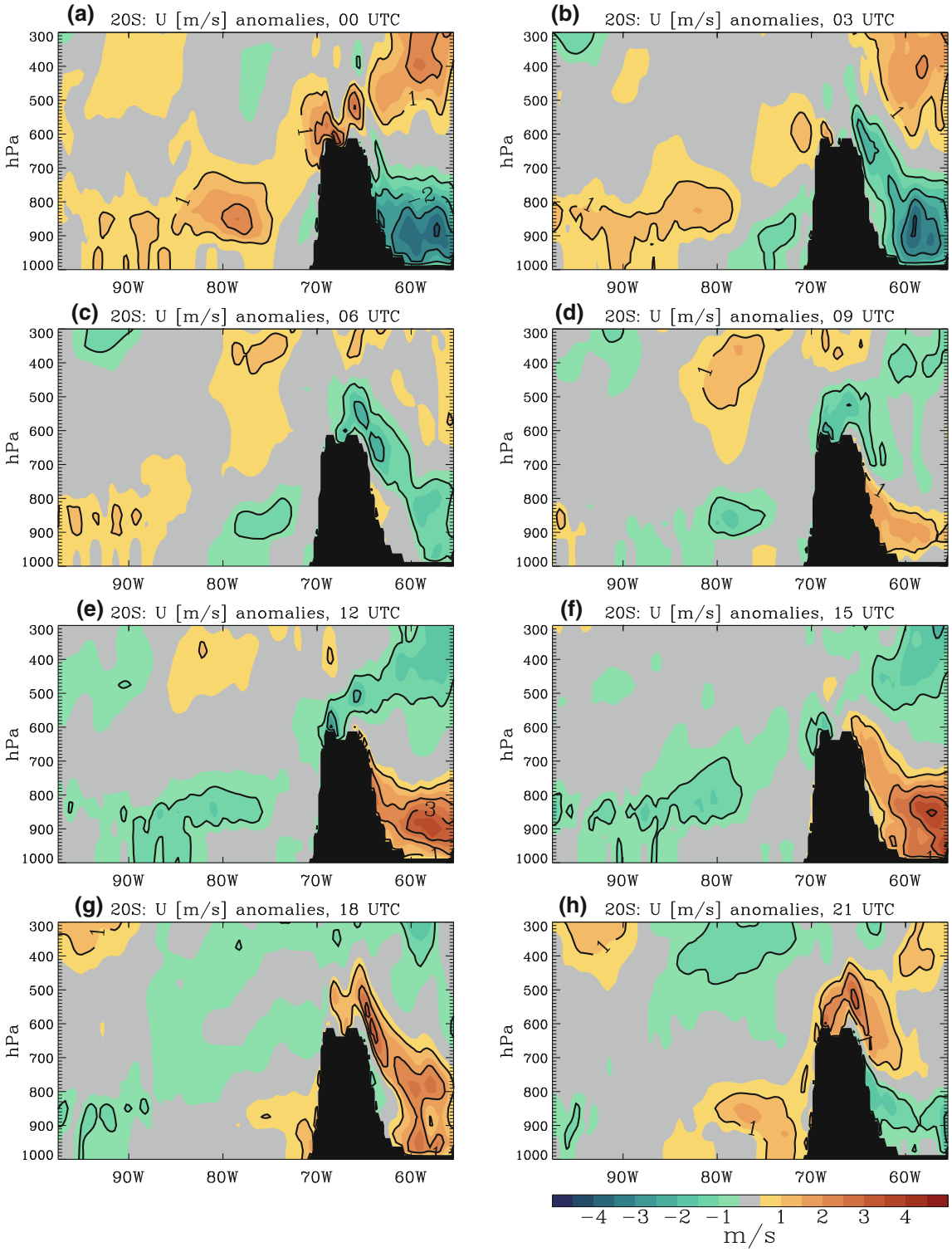

Fig. 5 Zonal wind anomalies across 20S latitude at three-hourly intervals for the mean diurnal cycle. Contour of ±1, ±2, ±3 and ±4 m/s are drawn

The semidiurnal component is largest along the Peruvian and Chilean coasts (Fig. 8b), as well as in areas approaching or poleward of 30S where a propagating diurnal wave is not supported (Rotunno 1983). Figure 8c, d depict the phases of the diurnal and semidiurnal harmonics of the horizontal mass divergence. The time of strongest subsidence (positive divergence anomalies) shows distinct propagation patterns. Subsidence over most of the ocean

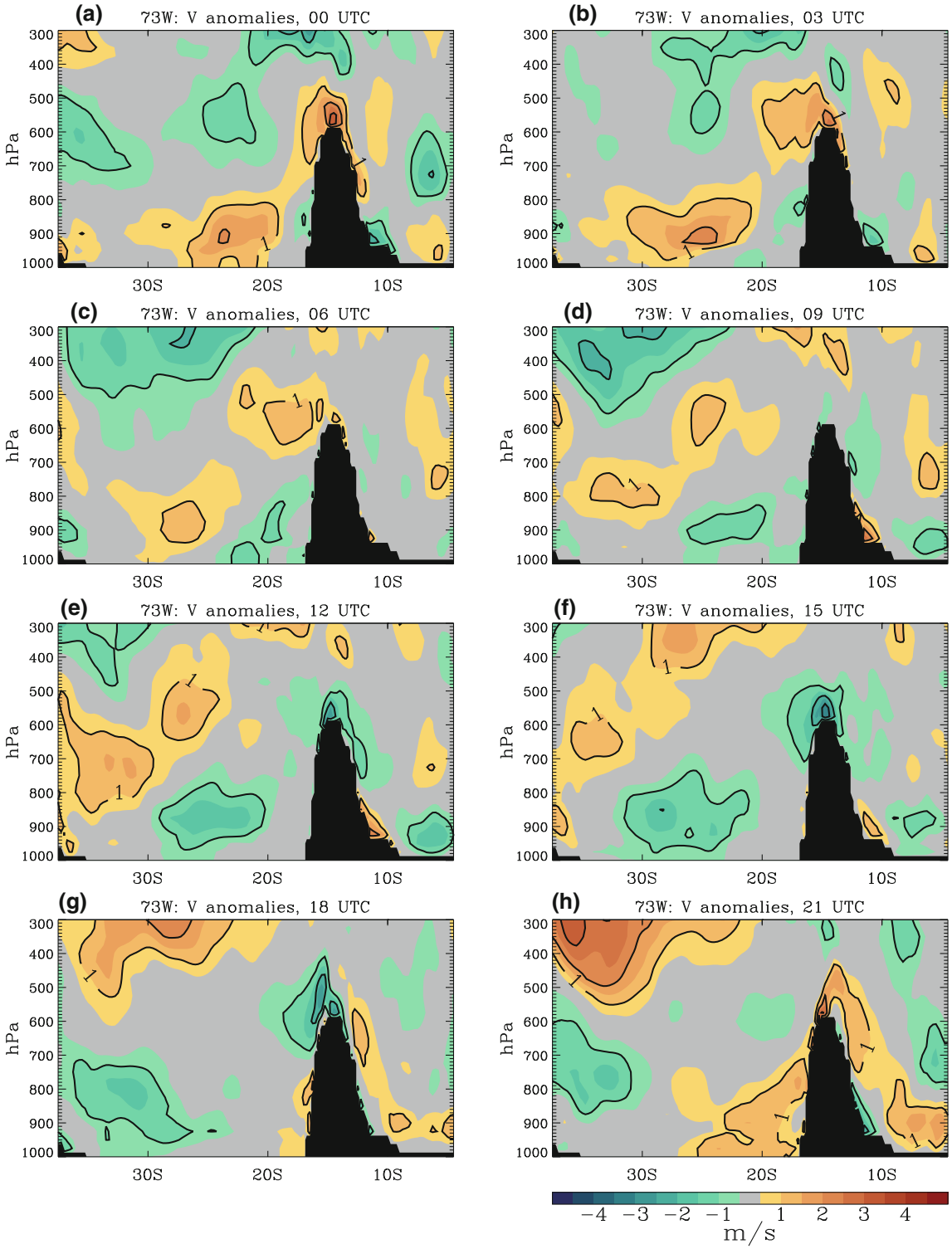

Fig. 6 Meridional wind anomalies across 73 W longitude at three-hourly intervals for the mean diurnal cycle. Contour of ±1, ±2, ±3 and ±4 m/s are drawn

away from the coasts peaks around 18:00–00:00 UTC (see also Fig. 7), which is reflected in the phase of the diurnal harmonic (Fig. 8c). Subsidence near the Peruvian coast peaks between 03:00–06:00 UTC (22:00–01:00 LT), and at progressively later times away from the coast. The diurnal harmonic is in phase with the semidiurnal one along the Peruvian coast; the latter component generally lags behind the former one moving away from the coast, as expected.

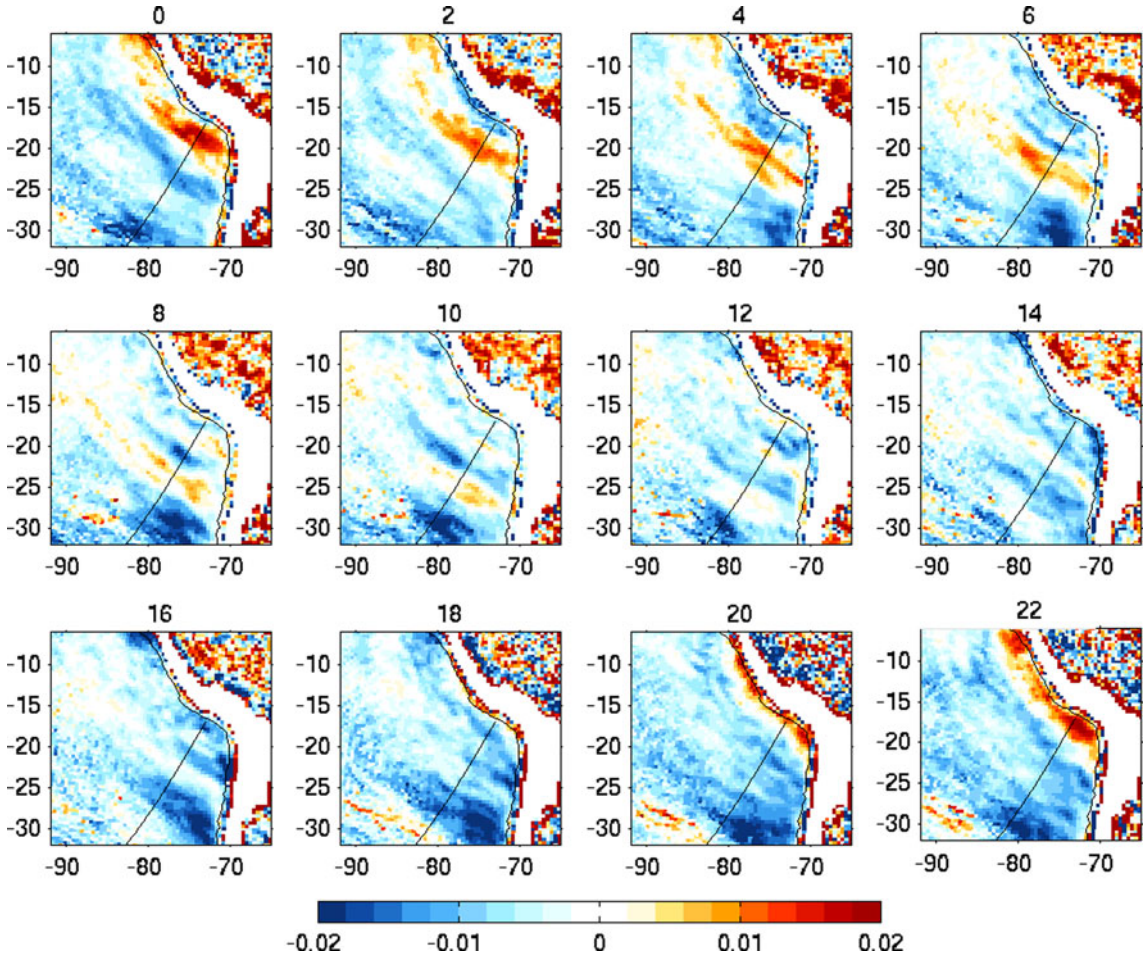

Fig. 7 Simulated mean vertical velocity (ms^{-1}) at 800 hPa at two hourly intervals for the mean diurnal cycle. UTC time is indicated above each panel. The *curved line* shows the transect utilised for the Hovmueller diagrams of Fig. 13

A similar peak time of the semidiurnal harmonic around 03:00–06:00 UTC (Fig. 8d) is apparent near the northern Chilean coastline. Here, phase-lines bend into a meridional direction. Taken together the features portrayed in Fig. 8 suggest the presence of two independent forcings of the divergence anomalies. In particular, the bands with enhanced semidiurnal amplitude and offshore propagation along the coast suggest an influence from land-sea and mountain breeze systems. Tropical breeze systems are characterised by convergence and divergence of the onshore wind component, and an out-of-phase along-shore wind oscillation (Rotunno 1983).

We investigate the split of the total anomalies into zonal and meridional contributions in Fig. 9, where the fractional variances associated with the diurnal and the semi-diurnal harmonics are shown for for each term. Diurnal zonal divergence anomalies tend to be dominant in the northern part of the SEP and away from the continent (Fig. 9a). Near the coast of northern Chile a strong diurnal component also corresponds with the variations of the low-level jet along the coast (Fig. 9b). The enhanced variance at the semi-diurnal frequency stems mainly from zonal divergence along the Chilean coast, and from meridional divergence along the Peruvian coast. This link with the coastal geometry lends further support to the notion that the semidiurnal component of the daily cycle is associated with land-sea breeze circulations.

4.2 Lower tropospheric anomalies at fixed locations

The diurnal rising and sinking waves originating from the coast leave their imprint on the circulation and stratification observed locally at oceanic stations. To examine these imprints, we show in Fig. 10 the vertical profiles of potential temperature at the WHOI and the DART buoy sites. At the WHOI buoy site, the diurnal cycle is most apparent around the MBL top at 850–900 hPa, where its amplitude exceeds 1.5 K and minimum values are between 09:00 UTC (3:00 LT) and 15:00 UTC (9:00 LT). The diurnal cycle is almost in-phase at all levels within the

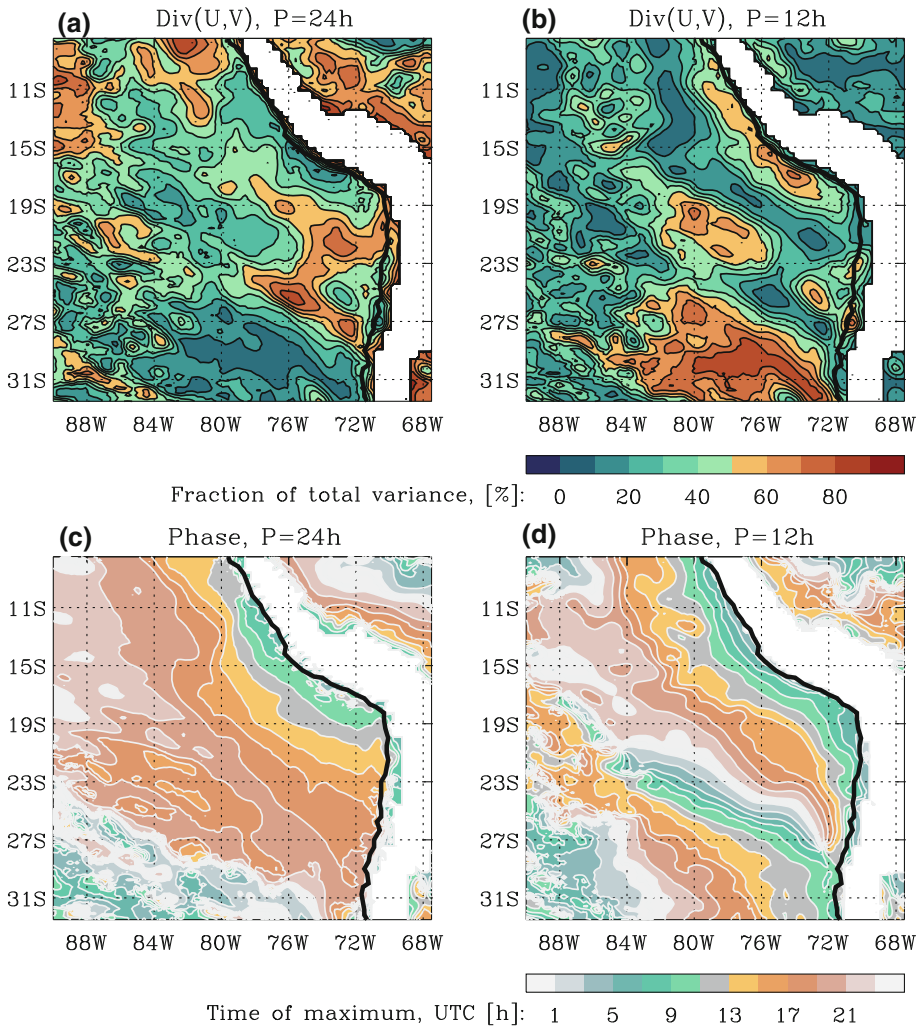

Fig. 8 Fractional variance of **a** diurnal and **b** semidiurnal components of the mean diurnal anomalies of the vertically integrated horizontal mass divergence between 1,000 and 800 hPa. **c**, **d** Their respective phases, indicated as the time of maximum vertical velocity

MBL with reduced amplitude. Above the MBL, the phase increasingly lags with height. This phase variation is indicative of thermal forcing in the MBL by the diurnal cycle of solar irradiation. At the DART buoy site, in contrast, the potential temperature profile displays a mixture of diurnal and semidiurnal signals. The diurnal cycle is similar to the one at the WHOI buoy site below 920 hPa, but no consistent phase lag with altitude is noticeable above that level. However, within the thin layer between 880 and 920 hPa that brackets the MBL top, the potential temperature displays an evident semidiurnal cycle. The amplitude of this semidiurnal cycle is about 1.2 K, with one peak at 09:00 UTC (04:00 LT) when anomalies locally forced by solar radiation are expected to be cold, and another peak at 00:00 UTC (19:00 LT). Above 880 hPa, the signal is a mixture of diurnal and semidiurnal components, with a single change in sign but more than two separate extrema. The second minimum and the positive maximum, in particular, are consistent with the radiatively forced diurnal cycle seen underneath the MBL top. We interpret the additional variations at 750 hPa and above the MBL top as the result of vertical advection of potential temperature caused by the two gravity-wave pulses emanating from the Peruvian and Chilean parts of the Andes.

4.3 Summary

Our model results indicate that the diurnal variability of the atmosphere in the SEP results from the superposition of both radiatively forced local signals and of remotely forced westward propagating signals. The latter signals first originate from the western slope of the Andes, and result from the ascending and descending motions caused by the daytime heating of the mountains. As the signals move away from the coast to the open ocean the remotely generated vertical wind anomalies might be either in phase, out of phase or phase lagged with those generated by local solar thermal forcing. This can give rise to secondary extrema and a semi-diurnal cycle. As the waves gradually weaken and dissipate while propagating, a clear

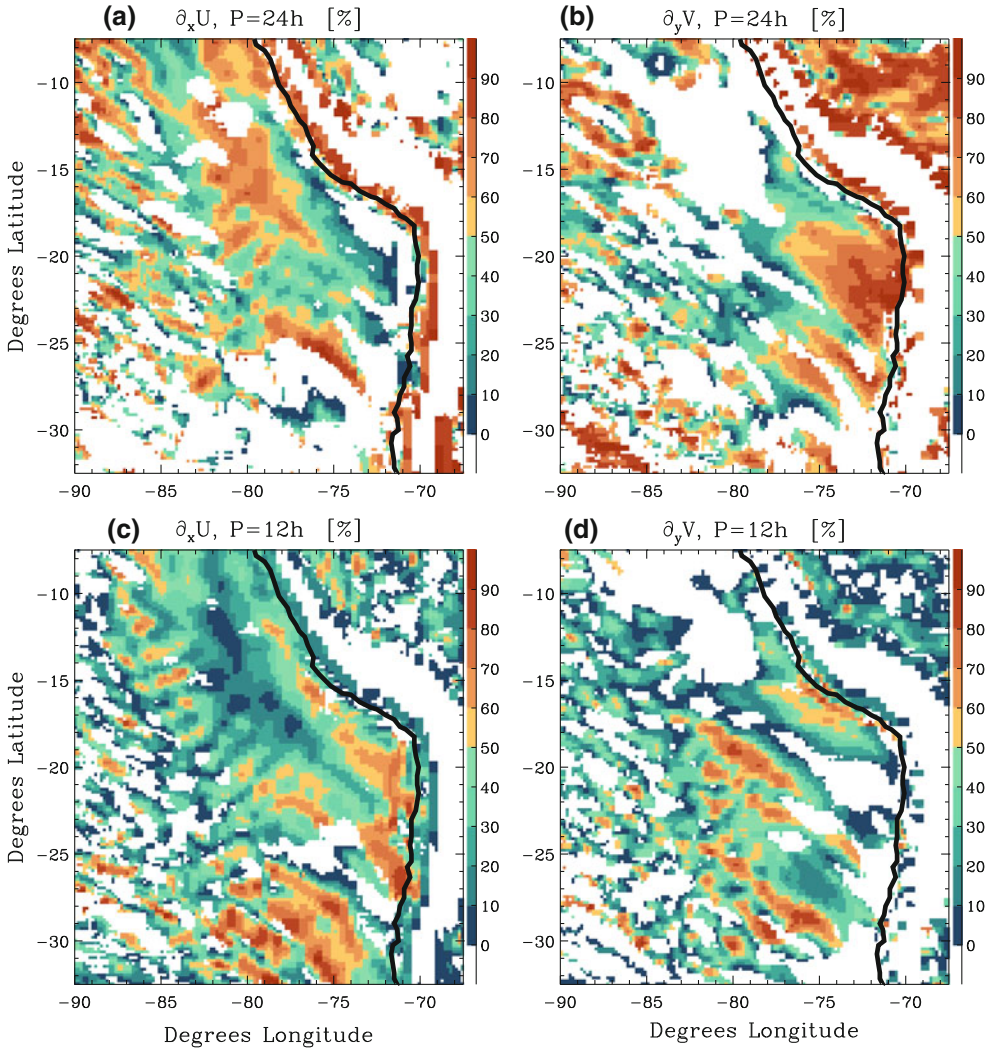

Fig. 9 Fractional variance (in %) of diurnal (**a**, **b**) and semidiurnal (**c**, **d**) components of zonal (**a**, **c**) and meridional (**b**, **d**) horizontal mass divergence, integrated between 1,000 and 800 hPa. Areas where the phase of the zonal/meridional divergence and is not within 45° of that of the total divergence are *left blank*

semidiurnal signal appears only in proximity of the land mass, as seen in Figs. 8 and 9. We find clear evidence of at least two distinct diurnal waves emanating from the South American continent. These are likely to be arise from different generation mechanisms, which probably correspond to different dry and moist diurnal circulations associated with the orography in the Peruvian and Chilean sectors. We explore this hypothesis in the next section.

5 Sensitivity experiments

To address the roles that various sectors of the South American continent play in forcing the diurnal variability of the lower boundary circulation and thermal structures in the SEP we designed a suite of sensitivity experiments in which the model's eastern boundary is progressively moved west. The coloured lines in Fig. 1 show the domain boundaries of these experiments along with that of the control. Compared with control, Exp-Andes excludes the low-lying land areas of eastern South America. Exp-Peru also excludes the Chilean Cordillera and the Bolivian altiplano. In Exp-Ocean the model domain is purely oceanic to totally exclude land diurnal forcing.

In addition to integrations over these domains with prescribed boundary conditions updated every 6 h, we performed parallel integrations where the frequency of updating boundary conditions at the eastern boundary over land was reduced to 24 h (00:00 UTC). In this case, the driving fields were obtained by averaging those at 00:00, 06:00, 12:00 and 18:00 UTC. Such a procedure removes any residual boundary forcing at sub-daily time-scales. The results from this set of experiments, however, were only slightly different from those made with 6-hourly updating.

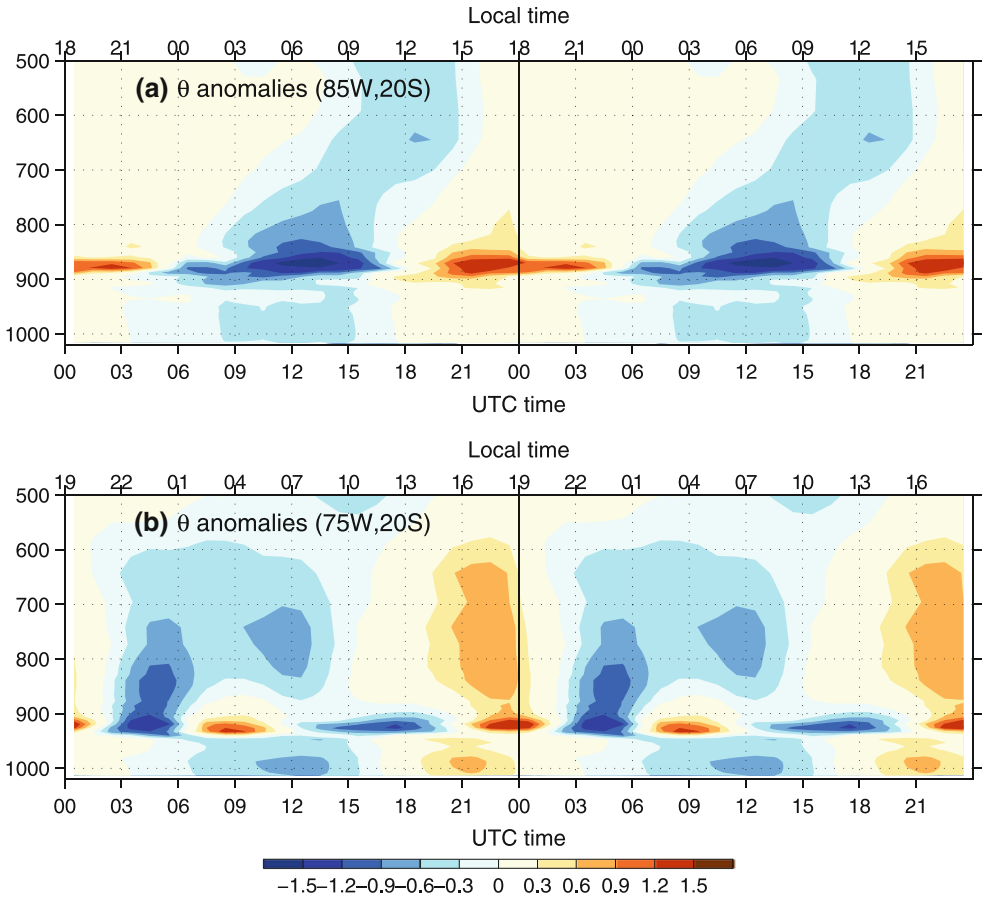

Fig. 10 Mean diurnal anomalies (long-term mean removed) of potential temperature (K) for the locations of the **a** WHOI buoy (85 W, 20S) and **b** DART buoy (75 W, 20S) in the control integration. The mean diurnal cycle is repeated twice

The eastern boundary conditions, therefore, provided very little diurnal forcing. In view of this result we do not discuss these parallel experiments any further. The results from the reduced-domain experiments for the diurnal cycle over the maritime area of interest here reflect a sensitivity to the forcing by circulations over the land areas that are represented within the model domain.

We first show in Fig. 11a the simulated mean vertical velocity at 800 hPa, just above the boundary layer, for the control integration. Figure 11b, c and d present the differences in diurnal mean vertical velocity between each of the reduced-domain simulations and the control (note the smaller range of the colour-bar compared with Fig. 11a). Exp-Andes shows relatively small differences with control, Exp-Peru has weaker subsidence in the southern part of the domain near the Chilean coast, and Exp-Ocean shows the weakening covering almost the entire eastern side of the domain. This weakening suggests, on the one hand, that the low-lying land areas of eastern South America exert a minor influence on the circulation over the marine domain to the west, and on the other hand, that the high Andes do impact the mean circulation over the southeast Pacific circulation, with possible consequences on the diurnal variability there.

Let us consider the diurnal cycle of the vertical wind at 800 hPa in the sensitivity experiments. In Exp-Andes, the diurnal cycle is very similar to control in both propagation pattern and intensity. Figure 12 shows maps of vertical velocity anomalies for Exp-Peru. An evident band of ascending motion propagates perpendicularly from the Peruvian coast to the open ocean. The timing of this wave front is very similar to that in control, first appearing along the coastline around 18:00 UTC and then peaking at around 22:00 UTC. The amplitude of the ascending wave is reduced somewhat compared to control, but its general propagation pattern is unchanged. This points to the primary role of the Peruvian Andes in generating the diurnal variability of the circulation in the lower troposphere. At the same time, semi-diurnal variations (visible in two bands at 8:00–10:00 UTC in Fig. 7) appear to be suppressed, which suggests a role of the Chilean Andes in generating the sub-diurnal variations.

The Hovmueller diagrams of Fig. 13 allow a direct comparison between all four integrations and provide evidence of different responses in at least two independent components of the diurnal forcing to changes in the model domain. Shown are vertical velocity anomalies at 800 hPa along a great circle extending from the coast of southern

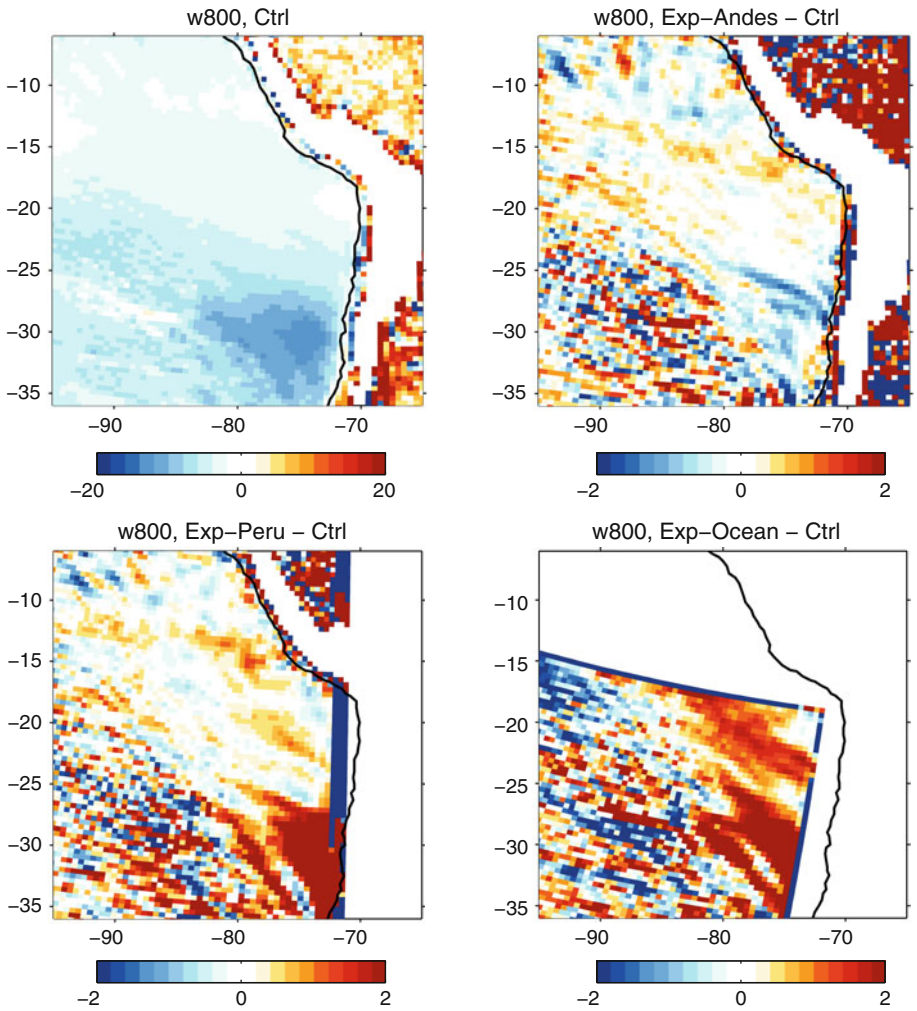

Fig. 11 Diurnal mean of vertical velocity (unit: mm/s) at 800 hPa of "Ctrl" (**a**) and the difference between the "Exp-Andes" (**b**), the "Exp-Peru" (**c**), and the "Exp-Ocean" (**d**) and the "Ctrl"

Peru (73 W, 17S) to about 2,300 km offshore at 85 W, 35S. In control several features can be distinguished. A main pulse of ascending motion peaks near the coast between 21:00 UTC and 23:00 UTC, consistently with the wave phases shown in Fig. 8c. This time corresponds to a sharp peak in deep-convective activity over the Peruvian lowlands (an area centred around 72 W, 15S) with a simulated rainfall intensity maximum of about 1 mm/h (not shown). The perturbation in vertical wind propagates southwestward with a nearly constant propagation speed of about 25 m/s, comparable with that reported in the EPIC 2001 field campaign (Bretherton et al. 2004), reanalysis data (Wood et al. 2009) and other modeling studies (Garreaud and Munoz 2004). The perturbation amplitude decreases gradually, but positive total (rather than just anomalous) vertical velocities associated with this pulse are found as far as about 2,000 km away from the coast, where large-scale subsidence prevails. Two additional propagating patterns of ascending motion with smaller amplitudes are also visible in the diagram, one appearing just away from the coast at around 06:00 UTC, the second, weaker still, peaking at the coast at 12:00 UTC. Both travel at a similar speed that is approximately half of that of the main pulse, indicating modes with higher vertical wavenumber. The first of these pulses is roughly synchronous with the main pulse and likely to be excited by the same event. Its amplitude maximum away from the coast may indicate downward wave propagation (see also Fig. 6b, c). The appearance of the second pulse at the coast corresponds instead with an eastward wind anomaly maximum at the foot of the orographic ridge (see Fig. 6c, d) and is associated with a mountain breeze. These secondary anomalies can generate secondary peaks at fixed locations (Fig. 8d) giving raise to a semidiurnal cycle. Their amplitude decreases quickly as they propagate and in our simulations they cause positive total vertical motion only out to about 600 km from the coast.

Compared to control, Exp-Andes (Fig. 13, second panel from the left) shows very similar diurnal pattern of vertical wind in timing, amplitude and propagation distance. This

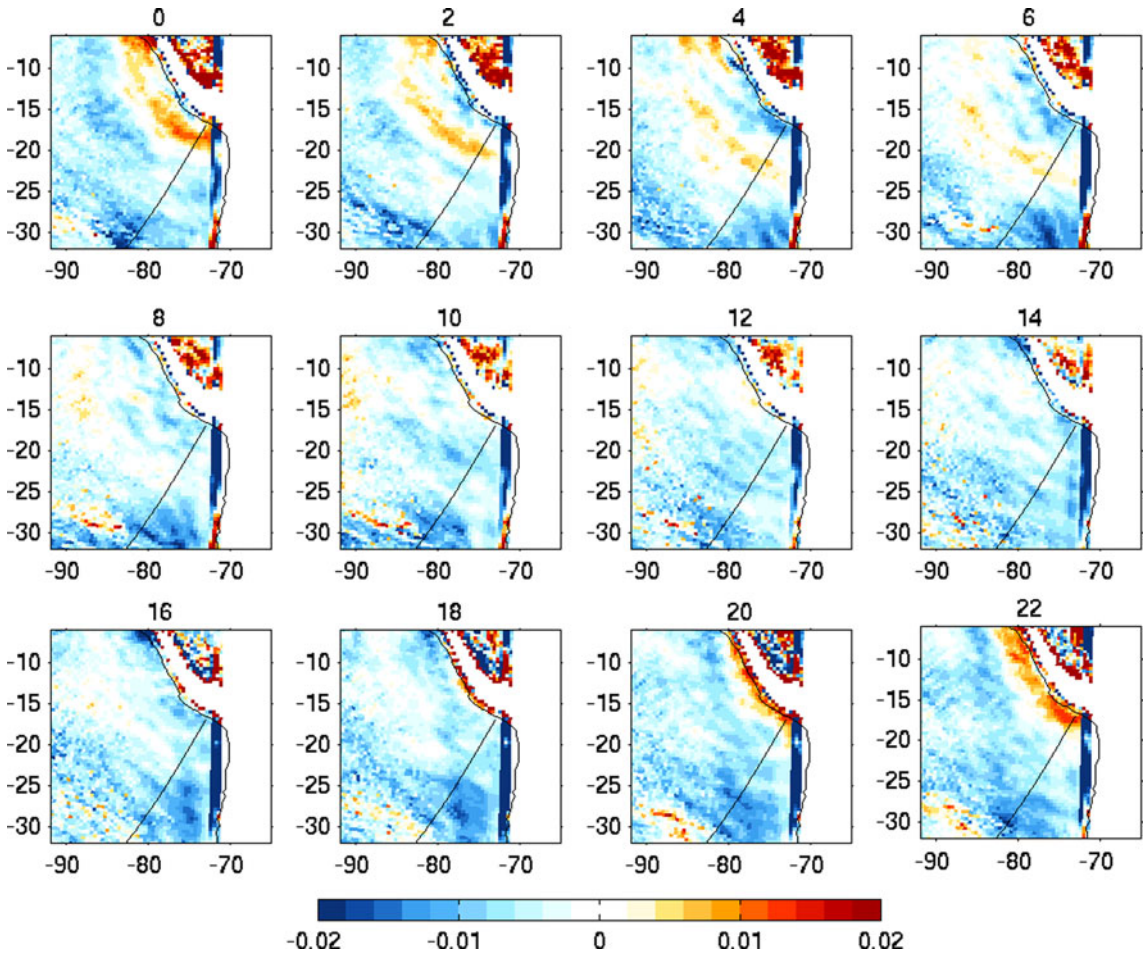

Fig. 12 Same as Fig. 7, but for Exp-Peru

similarity indicates that the direct impact of the more remote continental land areas east of the Andes on the coastal circulation of the western seaboard is rather small. By contrast, in Exp-Peru the main pulse of ascent, while unchanged in phase and propagation speed, has its amplitude reduced by about 40 %. As a result, the area of open ocean where mean diurnal variations result in upward vertical motion is reduced to only about one-half (out to 1,000 km distance from the coast) of that in control. Additionally, the secondary wave pulses, associated in the control with the semidiurnal cycle, are barely noticeable here. Finally, Exp-Ocean shows net subsidence over the whole oceanic domain, with residual weak ascent near the coast, and some alternation and propagation possibly forced in part by boundary inputs, and in part as a response to diurnal insolation.

According to these results, Exp-Peru constitutes a useful sensitivity test that helps isolating part of the diurnal forcing originating from the Peruvian and Chilean land masses. In particular the semidiurnal component, that appears associated with shallow land-sea and mountain breeze systems, is affected. The strongest signature of breeze systems in terms of vertical wind is expected to be found in the lower free troposphere just above the MBL. Figure 14 shows the changes in diurnal variability of vertically integrated horizontal mass divergence in the lower-troposphere (900–800 hPa) off the Chilean coast between 30S and 24S, and off the Peruvian coast between 18S and 15S (cf Fig. 14d). The selected domains are both characterized by strong low-level along-shore jets and alternating on-shore and off-shore winds forced by diurnal heating over the west- and south-westward facing slopes of the orography.

Let us first discuss the Peruvian sector (Fig. 14a), where the simulated diurnal cycles in control and Exp-Peru are similar to each other. Convergence is dominated by the onshore wind and occurs twice a day, with a main peak between 23:00 and 0:00 UTC, and a secondary one at 11:00 UTC. From the discussion of Fig. 13 we can associate these peaks with forcing by deep convection over land in the late afternoon and by a shallow density-driven mountain breeze blowing offshore in the early morning, respectively. In Exp-Peru both components are weaker than in control, but the difference is greater in the

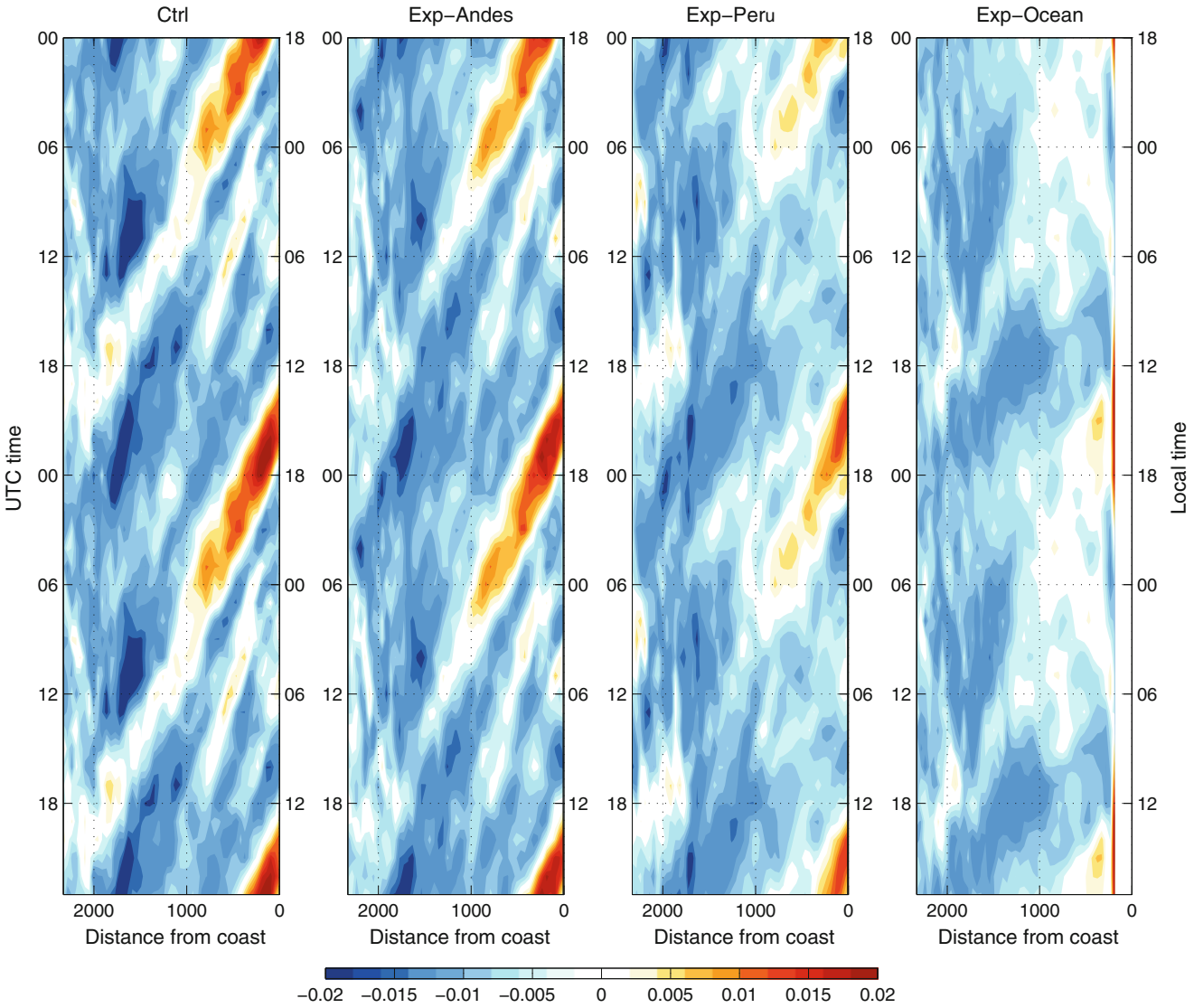

Fig. 13 Distance-time mean vertical velocity (ms^{-1}) at 800 hPa along the great circle between (73 W, 17S) and (85 W, 35S) for the control integration. The mean diurnal cycle is repeated twice. From *left* to *right*, the four panels show results from **a** the control integration, **b** Exp-Andes, **c** Exp-Peru, and **d** Exp-Ocean

breeze-induced anomaly, which is swamped by the divergent phase of the main wave. The along-shore wind has predominantly diurnal variations in both control and Exp-Peru, consistent with an approximately linear response to variations in the land-sea temperature contrast. Turning to the Chilean sector (Fig. 14b), we can see a dramatic difference between the two integrations, again mostly arising from the onshore (approximately zonal) wind component. Variations are predominantly semi-diurnal in control and diurnal in Exp-Peru. Similar arguments to those made for the Peruvian sector indicate that the anomalies between 00:00 and 06:00 UTC in Fig. 14b are forced by convergence over the orographic ridge (cf. Fig. 5b), while the second peak around 16:00 UTC, absent in Exp-Peru, is associated with an offshore breeze. The diurnally varying, geostrophic along-shore jet only has quantitative rather than qualitative differences between the two integrations. The semi-diurnal components of the on-shore flow divergence are isolated in Fig. 14c. This graph highlights the contrast between the relatively good agreement near the Peruvian shore and the marked weakening and phase difference of that component near the Chilean shore.

It is noteworthy that in control the divergence associated with the breeze systems off Chile has a three- to four-hour lag in reference to that off Peru (Fig. 14c). This is probably due to the different rates of heating of the terrain and the different geometrical properties of the topography. An additional cause may lie in interference between the wave emanating from Peru and the boundary-layer circulation anomalies over Chile. The eastern side of the semidiurnal

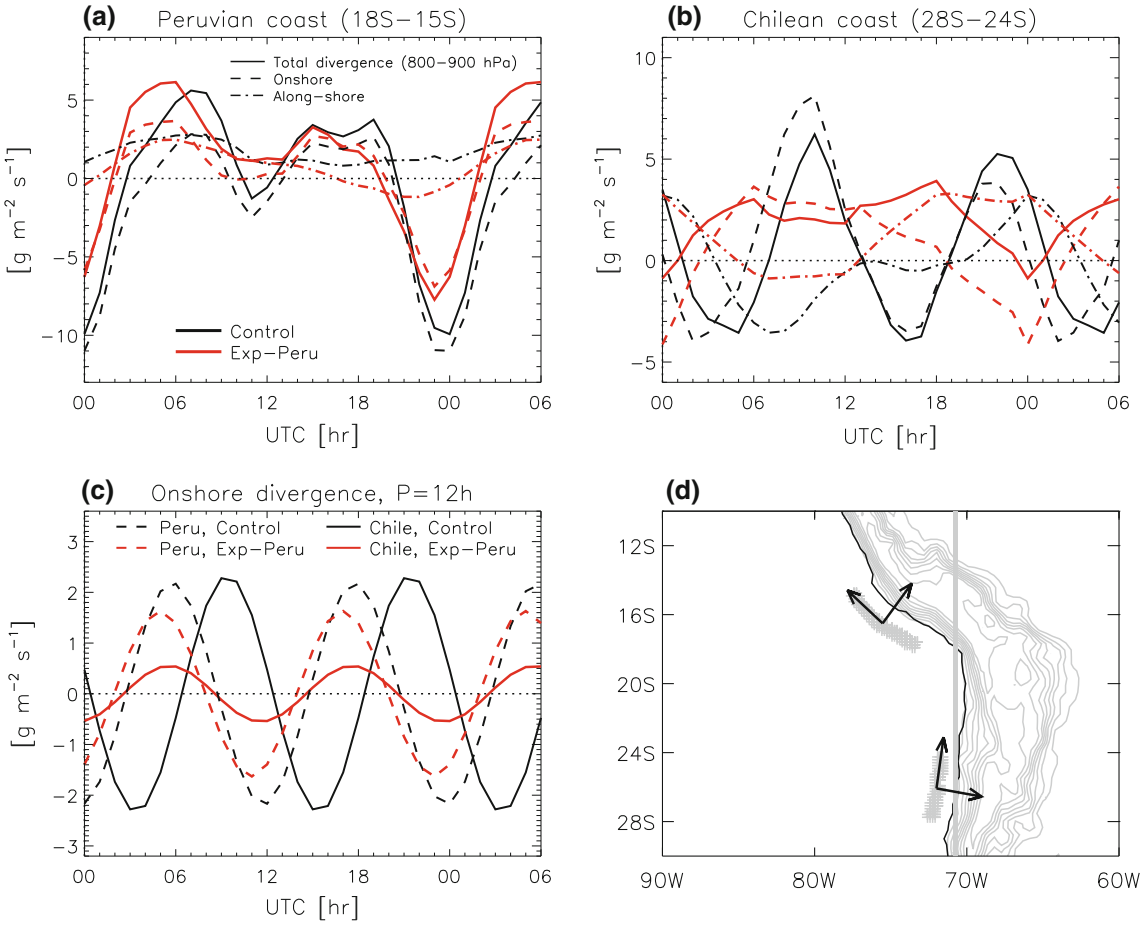

Fig. 14 Simulated mean diurnal cycle of horizontal mass divergence in the lower troposphere (900–800 hPa) along the **a** Chilean and **b** Peruvian shores. The values shown are averages for points lying over ocean between 100 and 150 km from the coast in the latitude ranges indicated. A graphic representation is given in panel (**d**). **a**, **b** Full lines show total horizontal divergence; *dashed* and *dash-dotted lines* refer to the divergence of the onshore and of the along-shore wind, respectively. Results from the control experiment are shown in *black*, those from Exp-Peru in *gray*. **c** 12-h period components of the on-shore components for each location and experiment

wave-front seen in Figs. 7 and 8 requires excitation from points near the Chilean land-mass roughly in phase with the Peruvian wave. In Exp-Peru, the 12-h components over the two near-shore locations are synchronised (Fig. 14c). With a travel time of about half a day for the Peruvian wave to reach the latitudes of the Chilean coast, the result is local destructive instead of constructive interference between the Chilean and the Peruvian waves which weakens the semidiurnal anomalies as seen in Fig. 13. The importance of this mechanism is supported by an experiment where the forcing at the eastern boundary is held constant at daily-mean values, the weakening of the semidiurnal anomalies is slightly less pronounced (not shown). Thus, not only the properties of the separate forcings over Peru and over Chile, but also the relative phase of the waves are significant for the diurnal cycle over locations in the SEP.

Finally, Fig. 15 shows the diurnal variability of vertical profiles of potential temperature at the WHOI and the DART buoy sites as simulated in the Exp-Peru experiment. Comparison with Fig. 10 shows that excluding the Chilean Cordillera from the simulation results in little qualitative differences at the WHOI buoy, but has major impacts at the DART buoy. Here, the vertical thermal structure shows a dominant diurnal harmonic, consistent with the diurnal forcing of solar irradiation. The disappearance of the semidiurnal component seen above the boundary layer top in Fig. 10b suggests that the diurnal rising and sinking waves that affect this location are primarily driven by effects of the Chilean Cordillera.

6 Robustness of the numerical simulation of the diurnal waves

The results shown in the previous sections are based on a configuration of the WRF model similar to that used in previous studies of the same region (Rahn and Garreaud

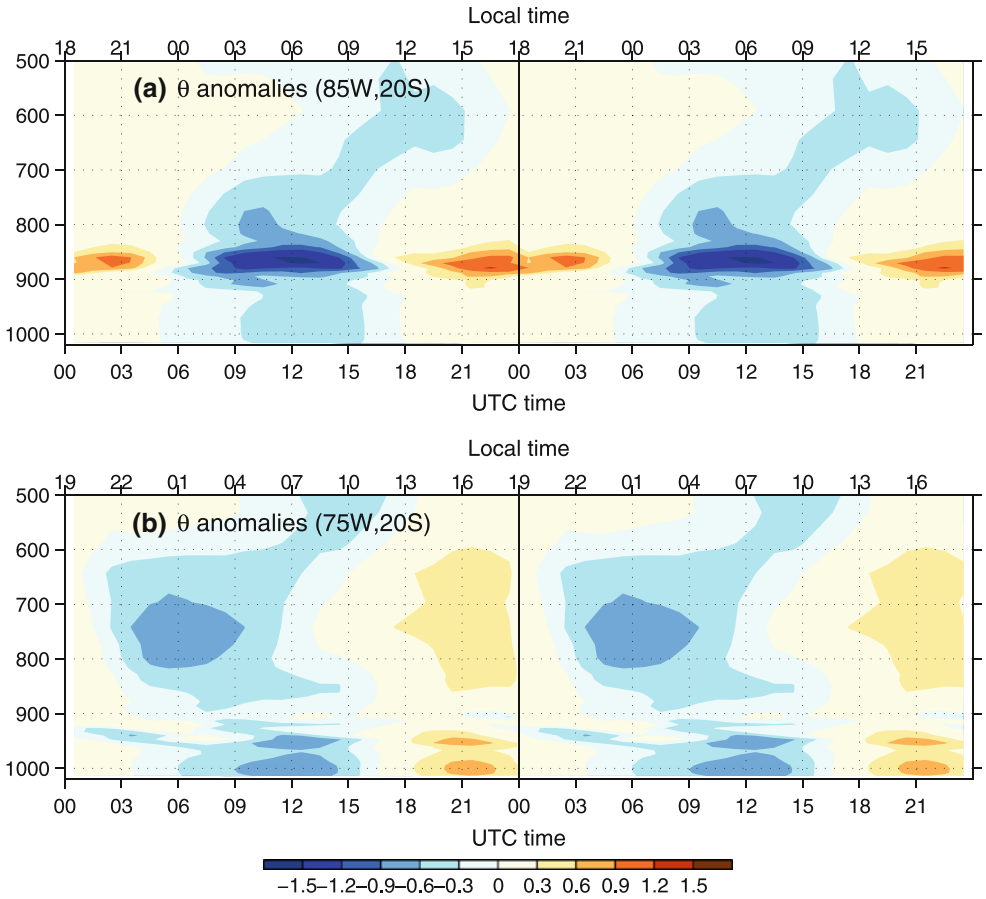

Fig. 15 Same as Fig. 10, but for Exp-Peru

2010a, b). In particular, the choice of vertical resolution from very fine (∼15 m) in the PBL to coarse in the mid-troposphere is in common with most previous investigations based on regional models (Garreaud and Ruttlant 2003; Garreaud and Muñoz 2005; Munoz 2008).

The question addressed in this study involves waves that are forced by diurnal circulations across the steep and tall orography of the Cordillera and propagate on the background of a circulation with a complex and highly variable vertical and horizontal structure. In addition, the high vertical refinement in the boundary layer is obtained at the price of a mismatch between the driving boundary conditions and the simulation in the interior domain. One outcome of such a mismatch is a spurious divergence near the domain boundary (see e.g. Fig. 11), which may provide an additional artificial forcing or reflection for gravity waves.

In order to explore the potential problems associated with boundary mismatches we designed additional simulations aimed to test the sensitivity of the results to the choice of model configuration. Our aim is to enable statements on the robustness of the results reported thus far by us as well as by other authors, and on the level of agreement that may be expected between numerical simulations and observations in this complex region of the atmosphere. The additional simulations were initialized not from the FNL analysis directly, but by a global-tropics WRF simulation with boundaries at 45S and 45 N. The horizontal grid of the tropical-channel domain matches FNL, while in the vertical a moderate refinement is used (from 29 to 35 or 52 w-levels). (In the following, we will refer to the vertical resolution with an "L" followed by the number of levels). Additional relaxation of the geopotential height towards FNL, with a 24-h time-scale, was applied in the domain interior to ensure that the observed mean climatology and global teleconnections were maintained. The hourly output from these integrations was then used as new boundary conditions for the SEP/South-American domain (35.5S–14 N, 111 W–31 W), simulated with three-fold horizontal and two-fold vertical refinement.

The L69 grid has improved resolution in the mid-troposphere, with a spacing of 25 hPa, but is coarser in the PBL than the control, L44 integration. With L103, the vertical resolution is more nearly uniform with a maximum spacing of less than 20 hPa and finer than both L44 and L69 grids everywhere. The numerical time-step was reduced to between 20 s and 1 min in these integrations, with radiative computations every 5 min. An additional, shorter integration with 123 levels was also performed, but

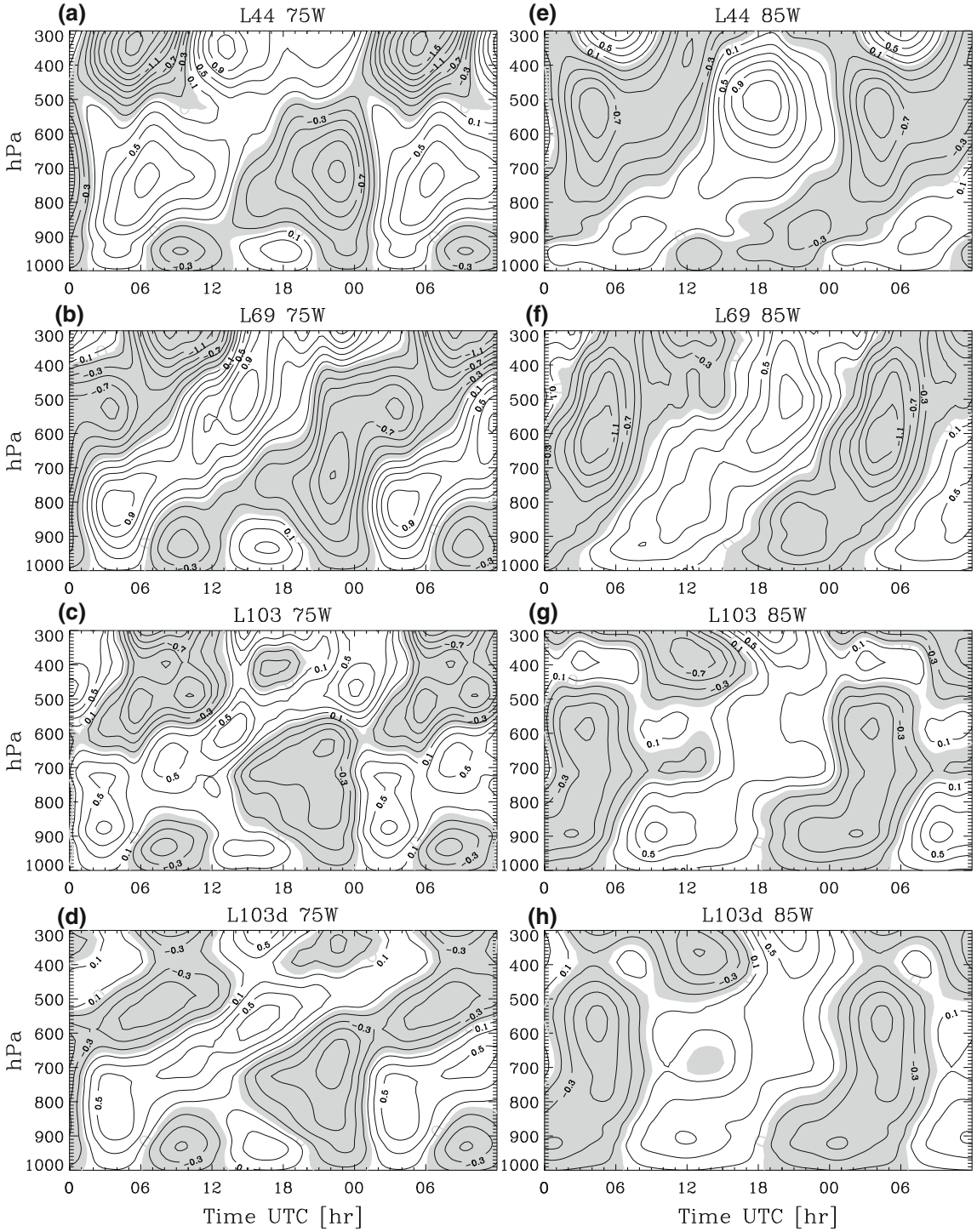

Fig. 16 Time-height Hovmueller diagrams for the simulated diurnal cycles at 20S, 75 W (*right*, **a**–**d**) and 20S, 85 W (*left*, **e**–**h**) in four different regional configurations of the WRF model. Contours indicate the vertical displacement from the mean, in hm, due to diurnal vertical velocity anomalies. Contour interval is 0.2 hm. *Shaded areas* indicate negative values

no significant additional differences from the 'L103' case could be seen.

Three L103 regional integrations were carried out for the month of October only. The first ('L103s') has a single domain, with 35 km resolution at 20S; the second ('L103') has an additional, two-way nested inner domain with three-fold horizontal refinement (11.6 km resolution at 20S) comprising the Peruvian and Andean Cordillera and the

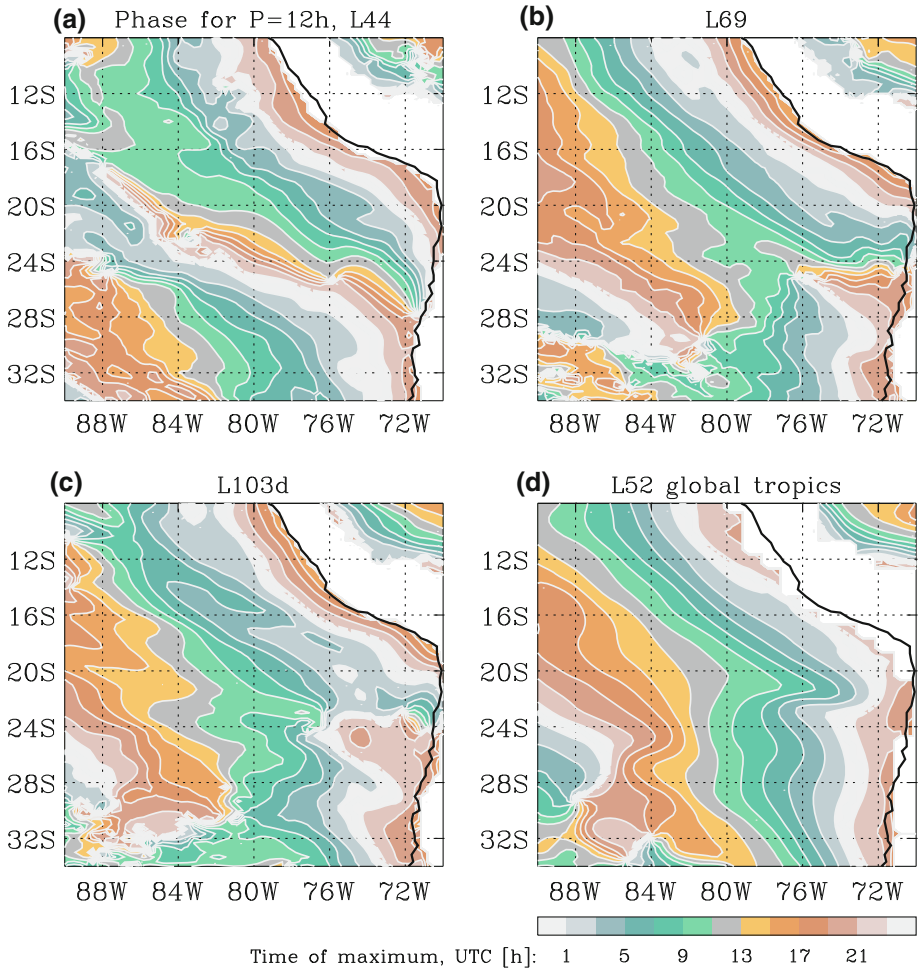

Fig. 17 Phase of the semi-diurnal component of the simulated mean daily vertical-velocity anomalies at 750 hPa in four different WRF configurations. The phase is given as the time of the maximum in hours UTC. *Blank areas* on land are for terrain with mean elevation greater than 750 hPa

coastal ocean out to 85 W; the third ('L103d') is similar to L103, except for a modified upper boundary (between 100 and 50 hPa) where vertical-velocity damping was applied to inhibit vertical wave reflection. The 69-level regional integration ('L69'), with configuration identical to L103 except for the vertical grid, was carried forward over 2 months, October and November. As before, model diagnostics for the last 15 days of October is considered; for the L69 case we also mention results for the second half of November. Interpolation onto 15 standard pressure levels and onto a common 1/3-degree latitude-longitude grid was performed prior to evaluation.

The main discrepancies among these experiments were found to be associated with the different choices of vertical grid. Horizontal refinement does not have a large impact on the diurnal wave over the ocean in the lower troposphere ($p > 500$ hPa). Few differences are seen when the resolution is increased from 35 to 11.6 km. Even at 1 degree resolution many results are qualitatively similar to those from the 1/3 degree integrations. In the following we limit the discussion to the L44 (control), the L69 and the L103 cases.

Figure 16 shows a comparison between the diurnal cycles at 20S, 75 W and 20S, 85 W in the four simulations, L44, L69, L103 and L103d. The values shown are averages over the 6 grid-points within 0.5 degrees of the desired locations. The diurnal vertical displacements over 1.5 cycles are shown, defined as the time-integrals of mean diurnal vertical-velocity anomalies, with the means removed to give a vanishing mean displacement. As a proxy for dynamically-induced temperature variations via the local stratification, this diagnostic gives greater emphasis to the gravity-wave component of the diurnal cycle compared to the diabatic part locally forced by insolation.

The agreement among the integrations is good at 75 W (Fig. 16a–d) in the lower part of the domain. There is a prominent semi-diurnal cycle with similar amplitude and a peak at 5UTC in all cases. Differences appear in the timing of the mid-day ($\sim$17UTC) maximum, which occurs 1 h earlier in L69 than in L44, and 1 h earlier still in L103. In the middle and upper troposphere, differences are much more marked. At 85 W (Fig. 16e–h), little agreement is found for the phase of the diurnal wave at all levels

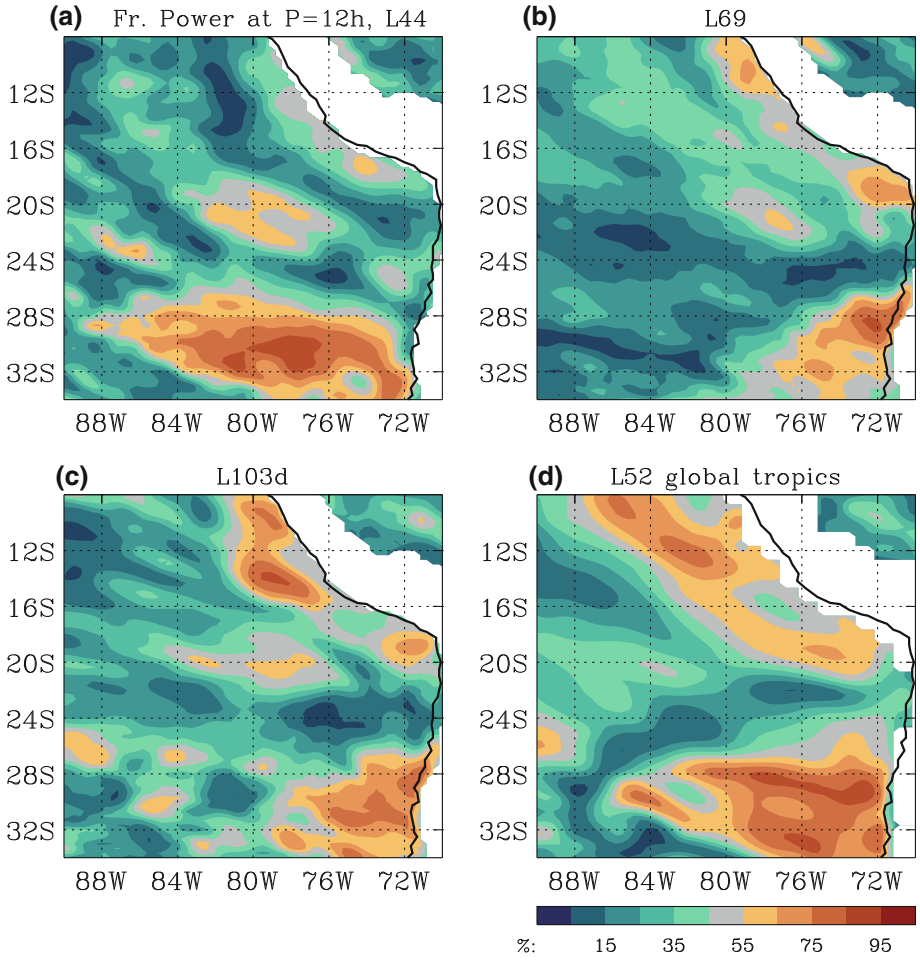

Fig. 18 Fraction of the total variance of daily vertical-velocity anomalies at 750 hPa associated with semi-diurnal period in the four integrations

between different simulations. The main impact appears to come from the vertical resolution. In particular, the downwelling phases in L44 and L103 are out-of-phase with each other. The effect of upper-boundary reflection (Fig. 16g, h) is mostly just a weakening of the low-level wave, with only minor phase changes.

Simulated phase errors have been ascribed to erroneous propagation speeds along the inversion, which is often too shallow in WRF simulations (Rahn and Garreaud 2010a). While the same comment can be made for our integrations, we find this is by no means the only or even the main potential source of phase errors. Figure 17 shows two-dimensional phase distributions of the 12-h component of the diurnal wave (at 750 hPa; the following is not sensitive to this choice of level), which is associated with much of the discrepancies between integrations. It is evident that the direction as well as the propagation speed of the main wave-front differs considerably between integrations. Phase differences along 20S are associated with different orientations of the front. In particular, L44 (Fig. 17a) shows the weakest zonal propagation. A stronger zonally-propagating component, more similar to L69 and L103/d, is also generated in the 52-level tropical-channel simulation (used to drive L103/d; Fig. 17d) where effects from nearby domain boundaries can be certainly excluded. The phase plots of Fig. 17b–d appear to be in better qualitative agreement with the results from operational analysis data (cf. Fig. 7b in Toniazzo et al. 2011). However, this cannot be taken to imply that the commonly used L44 set-up is intrinsically inferior to the other cases shown here, or its simulation of the diurnal wave less accurate. The mean inversion height, for example, is higher and thus better in L44. Also, at 20S, 85 W the timing of the diurnal phases appears in better agreement with available *in-situ* observation, even though these are affected by statistical uncertainties and do not separate thermodynamic and dynamic components. Within the scope of the present analysis we can only state that L44 displays a weaker coupling between waves at the inversion and in the middle and upper troposphere. While this can be ascribed to lower vertical resolution, there is no assurance that the modes that are represented in L69 or L103/d are correct.

The phase differences are accompanied by differences in power at the semi-diurnal frequency. Figure 18 shows that

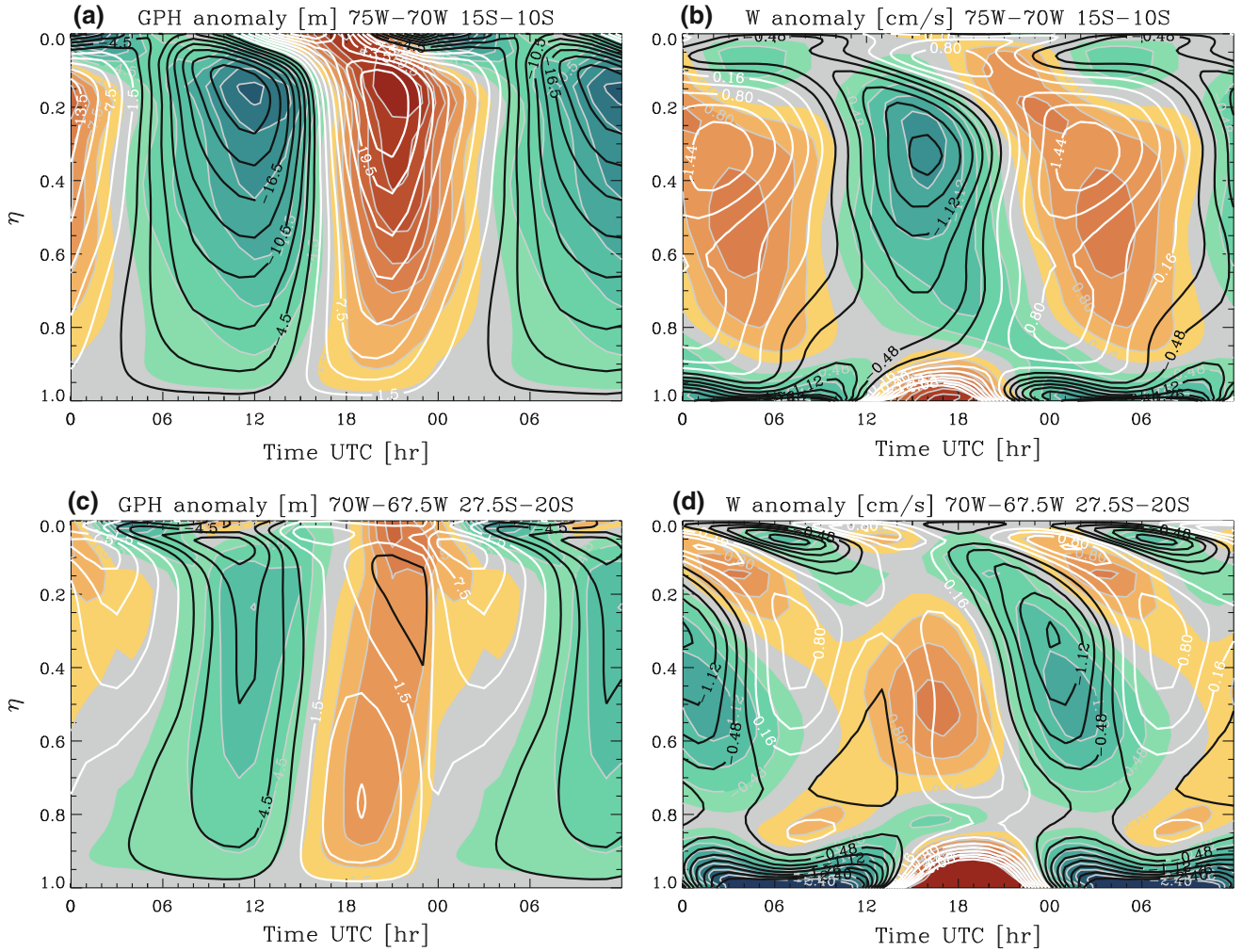

Fig. 19 Time-height Hovmueller diagrams of the mean daily anomalies of geopotential height (**a**, **c**) and vertical velocity (**b**, **d**) for areas over the Peruvian (**a**, **b**) and Chilean (**c**, **d**) Andes. The contour interval for GPH is 3 m, that of w is 0.32 cm/s. Colours are for the L44 simulation (*blue*/*red* for negative/positive values), and contour lines for the L69 case (*white* for positive values). The vertical coordinate is given as column mass fraction

L44 generally has less power near the coast, especially the Chilean. In Sect. 5 we showed that the semi-diurnal component near the coast is associated with convergence from the mountain breeze. Since this is a shallow circulation, changes in vertical resolution may have a greater impact on its representation than for the case of waves forced by deep convection. Correlation analysis (not shown) confirms that there is a weaker relationship in L44 between wind and pressure anomalies over the Andes and over adjacent ocean areas compared to the higher-resolution cases.

That such changes have also an impact on the phase is suggested by Fig. 19, comparing the diurnal anomalies over the southern Peruvian ridge in L44 (shown in colours) and in L69 (shown as contours; L103d very closely resemble L69 in this diagnostic). The ascent phase in L44 lags that in L69 by 1–2 h. These anomalies are deep and predominantly of diurnal frequency. Figure 19c, d show similar plots for the Chilean Andes. Here anomalous convergence is more sharply concentrated in the PBL in both simulations, and a stronger semi-diurnal component is apparent compared to the Peruvian ridge. However in L69 the vertical velocity (Fig. 19d) suggests vertical propagation, which appears weaker or absent in L44. The differences in the vertical structure of the anomalies are accompanied by a stronger semi-diurnal component in L69, especially at middle levels ($\eta = 0.6$–0.8). There is an earlier and sharper peak of the mid-level downwelling phase between 0 and 2 h UTC, followed by an upwelling phase with a peak at 9–10 UTC. The latter is almost absent in L44. In terms of anomalies in the geopotential height (Fig. 19c), this results in a delay of the negative phase by 1–2 h, and in a positive phase characterised by a higher vertical wavenumber.

A last comment pertains to the seasonality of the anomalies, which in the L69 simulation appears to be important. In this integration the diurnal waves in the second half of November have more power at the diurnal frequency than in October, and the wave-front appears to emanate mainly from the Peruvian orography. As expected, this is associated with more precipitation there, and with significant changes in the diurnal anomalies at fixed locations. This may constitute a confusing factor when comparing simulations with the observed mean daily cycle at stations where days from different periods of the year have been averaged together.

To summarise, some aspects of the diurnal variations in the SEP are simulated robustly with WRF. These are the presence of a main gravity-waves pulse that propagates west-to-southwestward over the coastal ocean with a phase speed of approximately 25 m/s and is forced by diurnal circulations over the Peruvian Andes. Additional variations are associated with waves forced by shallow coastal circulations, which emanate from both the Peruvian and the Chilean sector. However, the intensity of the different waves, their vertical structure, their phase, and their propagation speed and direction are all sensitive to the simulation set-up. In particular, it does not appear possible to make correct predictions on the precise timing of diurnal anomalies at a given location, or to calculate a reliable estimate of the distance that the upwelling wave travels before total vertical velocity remains negative at all times of the average day.

7 Conclusions

We have examined the diurnal anomalies of the atmospheric boundary layer circulation over the southeast Pacific using regional WRF model simulations. The model's ability to simulate the diurnal mean and mean diurnal variability was validated against *in-situ* observations and reanalysis products. The control integration produces a reasonably realistic simulation of the vertical temperature and humidity structures of the lower troposphere, and of the daily-mean boundary layer circulation and its diurnal variations. Notable biases include an overestimate of the strength of the surface winds and an underestimate of the atmospheric boundary layer height along the Peruvian-Chilean coast. Over open ocean areas biases are much reduced.

We decomposed the diurnal variability of the surface circulation into diurnal and semidiurnal harmonics, which together contain most of the total variance. In most oceanic areas, the diurnal component is generally dominant, but bands of strong semidiurnal variations appear parallel to the coastline and near the coast. The main band of enhanced semidiurnal amplitude in LWP is parallel to the Peruvian coastline, consistent with previous remote sensing studies (O'Dell et al. 2008). Above the inversion, vertical wind anomalies with a significant semidiurnal component are common, with increased amplitude near the coast.

The most prominent diurnal signal is associated with ascending motion following daytime heating of the west and south-westward facing slopes of the Andes. The main wave-front travels southwestward, away from southern Peru, over the open ocean, with an apparent phase speed of about 25 m/s, consistent with results from previous field campaigns, reanalysis and modeling studies (e.g., Bretherton et al. 2004; Wood et al. 2009; Garreaud and Munoz 2004; Rahn and Garreaud 2010a, b). This wave has a primarily diurnal character. Waves of semi-diurnal frequency also emanate from and propagate away from the continent, with a slower speed. Near the coast of Chile this component is the dominant one. Near the Equator, in a small fraction of our simulation domain, there are also contributions from the diurnal and semi-diurnal tides, consistent with the results of Takahashi (2012).

The impact of the wave on the PBL-top inversion over the ocean varies with location. In more remote ocean areas, the contribution from the gravity wave to the local diurnal variations, which are predominantly forced by local insolation, tends to be of secondary importance. At the site of the WHOI buoy (20S, 85 W) the anomalies associated with the gravity wave appear to be nearly in-phase with the solar component. At the site of the DART buoy (20S, 75 W), which is closer to the coast, dynamically forced anomalies are important and a mixture of diurnal and semidiurnal components is found.

We investigated the relative influences of South American land-masses on the simulated diurnal cycle. After verifying that boundary conditions alone do not provide the regional simulation with the necessary forcing to sustain the observed diurnal cycle, a main suite of sensitivity experiments was carried out with different horizontal domains that progressively exclude parts the South American continent where the gravity waves are forced. In Exp-Andes, the low-lying land areas to the east of the Andes are excluded. This results in negligible changes both for the mean structures and for the mean diurnal and semidiurnal components of the anomalies, indicating that the direct impact of the low-lying lands is rather small. By contrast, excluding the Chilean Andes from the computational domain in Exp-Peru results in significant differences. The amplitude of the upwelling gravity-wave pulse is reduced by about half. Near the coast of Chile, both the low-level meridional jet and the semidiurnal low-level convergence associated with the zonal land-sea breeze are substantially weakened and phase-shifted. This result is understood as a combination of missing or modified forcing

at the eastern boundary and interference with the Peruvian wave. In a further test, with all land points removed from the domain (Exp-Ocean), all semidiurnal variations are suppressed and permanent net subsidence occurs nearly everywhere.

These results from the simulations give a qualitative indication of the impact of different source regions of the Andes cordillera on the diurnal cycle over the SEP. Further tests showed, however, that it is not possible to make more stringent, quantitative statements. These include, for example, how far the upwelling gravity-wave travels before the total vertical wind stays negative (downward) at all times, which represents an important diagnostics for the estimation of impacts on the stratocumulus cloud. The reason for this uncertainty is that the simulated amplitude, phase, and propagation direction of the diurnal wave and its different components that affect such areas are not independent of model configuration. We found an especially strong sensitivity of the results to the choice of vertical grid. Our choice of WRF grid configuration for the control integration and for the sensitivity experiments ('L44', with 44 vertical levels most of which below 800 hPa) is similar to that of many previous simulations for this region (e.g. Rahn and Garreaud 2010a, b). In our experiments, this configuration shows a decoupling between low- and mid-tropospheric anomalies, with little vertical propagation. Over the steep terrain of the Andes, this also translates into poor horizontal propagation especially of shallow-forced anomalies. At least in part, this accounts for the weak amplitude of the semi-diurnal wave, which becomes more vigorous at higher and more uniform vertical resolution. The relative phase of the Peruvian and Chilean waves is also affected, changing the pattern of interference between them. Finally, the vertical resolution mismatch between the driving boundary conditions imposed from reanalysis products and the model grid, which is particularly large in L44, results in spurious forcing, such that standing-wave components can potentially be generated and the propagation of the wave-front misrepresented. We found indications that some convergence is achieved once the number of vertical levels is increased, gradually via progressive nesting, beyond 70. This alone however does not guarantee good agreement of the resulting simulation with observations.

Because of the combination of observational sampling uncertainties, the seasonal dependence of the diurnal cycle, and the complex concurrence of different generation mechanisms, direct comparison of the simulations with observations at a few fixed locations, such as at the two buoy sites along 20S, is of limited diagnostic use when attempting to discriminate between different numerical simulations.

To conclude, over the SEP the diurnal variability is the result of superposition of locally solar-induced diurnal cycle and remotely forced, propagating signals forced by the thermally direct circulations over the west- and southwest facing slopes of the Andes. A deep, 24-h wave is generated over the Peruvian orography, and moves southwestward, and a weaker, shallower wave with a significant semi-diurnal component propagates westward from the Chilean orography. These waves are primarily confined to the lower troposphere, and their impact on the inversion at the top of the marine boundary layer is substantial within 5 degrees from the coast. As they move towards the open ocean, the remotely generated down and upwelling waves can be either in phase, out of phase or phase lagged with respect to variation locally forced by solar radiation. Since the waves gradually disperse or dissipate while propagating, a clear semidiurnal signal appears only near coastal regions.

Acknowledgments Support for this study was provided by the NSF grant AGS-0747533 and U.S. DOE funding DE-SC0001467, and the UK NERC grant NE/F020465/1. The data were provided by the Research Data Archive (RDA), which is maintained by the Computational and Information Systems Laboratory (CISL) at the National Center for Atmospheric Research (NCAR). NCAR is sponsored by the National Science Foundation (NSF). The original data are available from the RDA (http://dss.ucar.edu) in dataset number ds083.2. The WRF model was developed at the National Center for Atmospheric Research (NCAR), which also provides training and support. WRF simulations in this research were supported in part by the National Science Foundation through TeraGrid resources provided by Pittsburgh Supercomputing Center, and by the Department of Meteorology at the University of Reading. ECMWF ERA-Interim data used in this study/project have been obtained from the ECMWF data server.

References

Bretherton CS et al (2004) The EPIC 2001 stratocumulus study. Bull Am Meteor Soc 85:967–977

Centre ERS d'Archivage et de Traitement (2002) QuikSCAT scatterometer mean wind field products user manual, version 1.0, Doc. C2-MUT-W-03-IF, Inst. Fr. De Rech. Pour l'Explor. de la Mer, Plouzané, France

Chen F, Dudhia J (2001) Coupling an advanced land-surface/hydrology model with the Penn State/ NCAR MM5 modeling system. Part I: model description and implementation. Mon Wea Rev 129:569–585

Dai A, Desser C (1999) Diurnal and semidiurnal variations in global surface wind and divergence fields. J Geophys Res 104: 31109–31125

Dee P, Uppala SM, Simmons AJ, Berrisford P, Poli P, Kobayashi S, Andrae U, Balmaseda MA, Balsamo G, Bauer P, Bechtold P, Beljaars ACM, van de Berg L, Bidlot J, Bormann N, Delsol C, Dragani R, Fuentes M, Geer AJ, Haimberger L, Healy SB, Hersbach H, Hlm EV, Isaksen L, Kllberg P, Khler M, Matricardi M, McNally AP, Monge-Sanz BM, Morcrette J-J, Park B-K, Peubey C, de Rosnay P, Tavolato C, Thpaut J-N, Vitart F (2011) The ERA-Interim reanalysis: configuration and performance of the data assimilation system. Q J R M S 137:553–597. doi:10.1002/qj.828

Deser C, Smith CA (1998) Diurnal and semidiurnal variations of the surface wind field over the tropical Pacific Ocean. J Clim 11(7):1730–1748

Dudhia J (1989) Numerical study of convection observed during the winter monsoon experiment using a mesoscale two-dimensional model. J Atmos Sci 46:3077–3107

Garreaud RD, Munoz R (2004) The diurnal cycle of circulation and cloudiness over the subtropical southeast Pacific: a modeling study. J Clim 17:1699–1710

Garreaud RD, Muñoz RC (2005) The low-level jet off the West Coast of Subtropical South America: structure and variability. Mon Wea Rev 133:2246–2261

Garreaud RD, Ruttlant J (2003) Coastal lows along the subtropical West coast of South America: numerical simulation of a typical case. Mon Wea Rev 131:891–908

Hong S-Y, Noh Y, Dudhia J (2006) A new vertical diffusion package with an explicit treatment of entrainment processes. Mon Wea Rev 134:2318–2341

Jet Propulsion Labortory (2000) QuikSCAT science data product, user's manual, overview and geophysical data products, version 2.0-draft, Doc. D-18053, California Institute of Technology, Pasadena, CA

Kain JS, Fritsch JM (1990) A one-dimensional entraining/ detraining plume model and its application in convective parameterization. J Atmos Sci 47:2784–2802

Ma H-Y, Mechoso CR, Xiao H, Wu C-M, Xue Y, De Sales F (2010) Connection between the South Pacific anti-cyclone, Peruvian Stratocumulus, and the South American Monsoon System. CLIVAR Exchanges

Mapes BE, Warner TT, Xu M (2003) Diurnal patterns of rainfall in northwestern South America. Part III: Diurnal gravity waves and nocturnal convection offshore. Mon Wea Rev 131: 830–844

Medeiros B, Williamson DL, Hannay C, Olson JG (2012) Southeast pacific stratocumulus in the community atmosphere model. J Clim. doi:10.1175/JCLI-D-11-00503.1

Minnis P, Harrison EF (1984) Diurnal variability of regional cloud and clear-sky radiative parameters derived from GOES data. Part II: November 1978 cloud distribution. J Clim Appl Meteor 23:1012–1031

Mlawer EJ, Taubman SJ, Brown PD, Iacono MJ, Clough SA (1997) Radiative transfer for inhomogeneous atmosphere: RRTM, a validated correlated-k model for the long-wave. J Geophys Res 102 (D14):16663–16682

Munoz RC (2008) Diurnal cycle of surface winds over the subtropical southeast Pacific. J Geophys Res 113:D13107

O'Dell CW, Wentz FJ, Bennartz R (2008) Cloud liquid water path from satellite based passive microwave observations: a new climatology over the global oceans. J Clim 21:1721–1739. doi: 10.1175/2007JCLI1958.1

Rahn DA, Garreaud R (2010a) Marine boundary layer over the subtropical southeast Pacific during VOCALS-REx – Part 1: mean structure and diurnal cycle. Atmos Chem Phys 10: 4491–4506. doi:10.5194/acp-10-4491-2010

Rahn DA, Garreaud R (2010b) Marine boundary layer over the subtropical southeast Pacific during VOCALS-REx – Part 2: synoptic variability. Atmos Chem Phys 10:4507–4519. doi: 10.5194/acp-10-4507-2010

Reynolds RW, Smith TM (1994) Improved global sea surface temperature analyses. J Clim 7:929–948

Rodwell MJ, Hoskins BJ (2001) Subtropical anticyclones and summer monsoons. J Clim 14:3192–3211

Rotunno R (1983) On the linear theory of the land sea breeze. J Atmos Sci 40:1999–2009

Rozendaal MA, Leovy CB, Klein SA (1995) An observational study of diurnal variations of the marine stratiform clouds. J Clim 8:1795–1809

Rutllant J (1993) Coastal lows and associated southerly winds in north-central Chile. Preprints, Fourth international conference on Southern Hemisphere Meteorology, Hobart, Australia. Am Meteor Soc, pp 268–269

Skamarock WC, Klemp JB, Dudhia J, Gill DO, Barker DM, Duda MG, Huang X-Y, Wang W, Powers JG (2008) A description of the Advanced Research WRF Version 3. NCAR Tech. Note NCAR/TN-475 + STR, June 2008, 125 pp

Takahashi K (2012) Thermotidal and land-heating forcing of the diurnal cycle of oceanic surface winds in the eastern tropical pacific. Geophys Res Lett 39 (4). doi:10.1029/2011GL050692

Toniazzo T, Abel SJ, Wood R, Mechoso CR, Allen G, Shaffrey LC (2011) Large-scale and synoptic meteorology in the south-east Pacific during the observations campaign VOCALS-REx in austral Spring 2008. Atmos Chem Phys 11:4977–5009. doi: 10.5194/acp-11-4977-2011

Wood R, Bretherton CS, Hartmann DL (2002) Diurnal cycle of liquid water path over the subtropical and tropical oceans. Geophys Res Lett 29:2092. doi:10.1029/2002GL015371

Wood R, Köhler M, Bennartz R, O'Dell C (2009) The diurnal cycle of surface divergence over the global oceans. Quart J R Meteorol Soc 135(643):1484–1493

Wyant MC, Wood R, Bretherton CS, Mechoso CR, Bacmeister J, Balmaseda MA, Barrett B, Codron F, Earnshaw P, Fast J, Hannay C, Kaiser JW, Kitagawa H, Klein SA, Khler M, Manganello J, Pan H-L, Sun F, Wang S, Wang Y (2010) The PreVOCA experiment: modeling the lower troposphere in the Southeast Pacific. Atmos Chem Phys 10(10):4757–4774. doi: 10.5194/acp-10-4757-2010

Yang Q, Gustafson WI Jr, Fast JD, Wang H, Easter RC, Morrison H, Lee Y-N, Chapman EG, Spak SN, Mena-Carrasco MA (2011) Assessing regional scale predictions of aerosols, marine stratocumulus, and their interactions during VOCALS-REx using WRF-Chem. Atmos Chem Phys 11:11951–11975